41st Aerospace Sciences Meeting and Exhibit
6-9 January 2003, Reno, Nevada

AIAA 2003-1266

Numerical Simulations of Transient Growth in a Mach 15 Boundary Layer over a Blunt Leading Edge

Haibo Dong *and Xiaolin Zhong †
University of California, Los Angeles, California 90095

Abstract

The receptivity process of hypersonic boundary layer flows over blunt leading edges has been paid more attentions in recent years. After free stream disturbances pass through and interact with the bow shock, three kinds of transmitted waves will be generated and interact with the boundary layer on the body during propagation to downstream. This generated complex wave field behind the bow shock will lead linear eigenmode growth or transient growth of perturbations inside boundary layer. Due to the progress of computer techniques, direct numerical simulation (DNS) has recently become a powerful tool to study the stability and transition of compressible boundary layers. In this paper, parametric simulations of receptivity to freestream disturbances including fast acoustic waves, vorticity waves and entropy waves for Mach 15 flow over 3-D blunt leading edges have been carried out by using high-order finite difference method on parallel computers. The results show that initial transient growth of instability waves generated and developed inside the hypersonic boundary layer near the leading edge can be observed in the receptivity of freestream standing vorticity waves or entropy waves, but not acoustic waves or other traveling waves. It is also shown that this initial transient growth near the leading edge can be possibly explained by the "transient growth" theory. Additionally, spanwise wave number effects, $y-z$ angle φ effects, nonlinearity effects, wall temperature effects on the instability growth are studied in the receptivity of streamwise vorticity waves. Effects of inhomogeneous boundary conditions or low-amplitude random distributed roughness on the surface are investigated in this paper, too.

1 Introduction

The prediction of laminar-turbulent transition in hypersonic boundary layers is a critical part of the aerodynamic design and control of hypersonic vehicles. The transition process is a result of nonlinear response of laminar boundary layers to forcing disturbances [1], which can originate from many different sources including free stream disturbances, surface roughness and vibrations [2]. In an environment with weak initial disturbances, the path to transition consists of three stages: 1) receptivity, 2) linear eigenmode growth or transient growth, and 3) nonlinear breakdown to turbulence.

The first stage is the receptivity process [3], which converts the environmental disturbances into initial instability waves in the boundary layers. Theoretical results on incompressible boundary layer receptivity are mainly obtained based on the asymptotic theory [4,5]. The asymptotic analysis explains how the long wavelength free stream acoustic disturbances enter the boundary layer and generate short-wavelength Tollmien-Schlichting (T-S) waves in incompressible boundary layers. The receptivity mechanism provides important initial conditions of amplitude, frequency, and phase of instability waves inside the boundary layers. Direct numerical simulation (DNS), which numerically solves the full Navier-Stokes equations as an initial-boundary problem, has become an important tool in receptivity and transition studies recently. The direct numerical simulation of the receptivity of incompressible boundary layers has been performed by Murdock [6]; Lin, Reed, and Saric [7]; Buter and Reed [8]; and Collis and Lele [9].

The stability and transition of supersonic and hypersonic boundary layers was reviewed by Mack [10], Morkovin [11], Arnal [12], and Reed and Saric [13]. For hypersonic boundary-layer flows over blunt bodies, the receptivity phenomena are much more complex and are currently not well understood [11,14]. Figure 1 shows a schematic of wave interactions in the leading edge region of a hypersonic flow in the presence of free stream disturbances. The receptivity phenomena are altered considerably by the bow shock in front of the body. The interaction of free stream waves with the shock affects the receptivity process of the boundary layer behind the shock. Kovasznay [15] showed that weak disturbance waves in compressible flow can be decomposed into three independent modes: acoustic, entropy, and vorticity modes. The acoustic wave is propagated with the speed of sound relative to the moving fluid, while the entropy and vorticity waves convect with the moving fluid velocity.

The second stage is the subsequent linear de-

*Ph.D., Mechanical and Aerospace Engineering Department, Student Member AIAA, haibo@seas.ucla.edu

†Professor, Mechanical and Aerospace Engineering Department, Associate Fellow AIAA, xiaolin@seas.ucla.edu.

velopment and growth of boundary-layer instability waves. Relevant instability waves for hypersonic boundary layers include the first mode and higher mode instability [10], the Görtler instability over concave surfaces [16], attachment line instability in leading edges, and cross flow instability in three-dimensional boundary layers [13]. Most of our knowledge on the stability properties of hypersonic boundary layers is obtained by the analysis of local parallel linear stability theory (LST) [10,17,18]. Lees and Lin [19] showed that the existence of a generalized inflection point is a necessary condition for inviscid instability of a compressible boundary layer. Mack [10] found that there are higher acoustic instability modes in addition to the first-mode instability waves in supersonic and hypersonic boundary layers. Among them, the second mode becomes the dominant instability for hypersonic boundary layers at Mach numbers larger than about 4. The existence and dominance of the second mode have been validated by experimental stability studies [12,20].

Another possible second stage of the transition process is "transient growth" mechanism, which was first identified by Ellingsen and Palm [21] and Landahl [22], and since its discovery, a number of investigators have contributed to its basic theoretical understanding [23,24]. The basic idea is that transient growth arises from a coupling of oblique T-S and Squire modes that exists because the linearized Navier-Stokes equations are not self adjoint and therefore have nonorthogonal eigenmodes. Thus, even when all the eigenmodes are damped, some transient period of algebraic growth occurs prior to the eventual exponential decay of the disturbances. Recently, theoretical work in this area by Andersson et al. [25], Lunchini [26], Butler and Farrell [27] and Tumin and Reshotko [28] has addressed spatial transient growth in 2-D boundary layers. Andersson et al. and Luchini consider the growth of stationary disturbances in non-parallel Blasius boundary layers at finite and infinite Reynolds numbers, respectively. Tumin and Reshotko consider the more general case of arbitrarily oriented disturbances at nonzero frequencies but are restricted to parallel-flow boundary layers. In all cases, the optimal disturbances is shown to be a streamwise-oriented vortex that produces a longitudinal streak downstream. Tumin and Reshotko also verified that zero frequency disturbances undergo more growth than unsteady disturbances. Consideration of "transient growth" has lead to an enlargement and clarification of the paths to transition by Morkovin, Reshotko, and Herbert [29]. Figure 2 shows the receptivity mechanism summarized by Morkovin, Reshotko, and Herbert. Upon on their clarification, there are five possible paths to transition. Among those paths, transient growth may provide a higher amplitude to the eigenmode growth upon crossing into an exponentially unstable region. If the transition growth is large enough, it could directly excite secondary instabilities and mode interactions. Therefore, transient growth is considered as a candidate mechanism for many examples of bypass transition.

Recently, there has been renewed interest in the surface roughness problem, too. Often, in configurations with moderate to large-amplitude surface roughness, transition occurs in the Reynolds number region subcritical to the exponential growth of Tollmien-Schlichting (T-S) waves. The mechanism that produces this subcritical, roughness-induced transition has not been conclusively identified and has therefore been labeled as an instance of "bypass transition". Berry et al. [30] have done a experimental study of roughness effects on the Orbiter at NASA Langley Research Center in hopes of developing a better predictor of transition behavior since the Orbiter occasionally experiences boundary layer transition earlier than nominal due to surface roughnesses that result from the relatively fragile nature of the thermal protection system ceramic tiles. Reshotko [24] also analytically studied the problem of the "blunt body paradox", which refers to the early transition on spherical forebodies observed at supersonic and hypersonic freestream flows. Even the surface is smooth, this transition still occurs in the subsonic portion of the flow behind the bow shock, a region of highly favorable pressure gradient that is stable to T-S waves. Surface cooling leads to even earlier transition. The tentative suggestions are generally roughness related since stagnation point boundary layers are very thin under such flow conditions. Recently, White and Reshotko [31] did a new experimental work that provides the first experimental investigation of the link between roughness and transient growth on a flat plate. In their work, the nominal freestream speed of the experiments is $8m/s$. Four kinds of surface roughnesses, low-amplitude roughness, isolated roughness element, roughness array, and moderate-amplitude roughness are used in their experiments. Their results indicate that under certain circumstances, the behavior of roughness-induced disturbances is consistent with transient-growth theory. Acutually, via "transient growth" mechanism, the disturbances that grow to the largest amplitudes are stationary(i.e. zero frequency) streamwise vortices, exactly those known to be produced by distributed surface roughness. This implies that "transient growth" may be the mechanism that leads to subcritical roughness-induced transition in hypersonic boundary layers.

In this paper, we extend our previous work to do parametric simulations of receptivity to freestream disturbances including fast acoustic waves, vorticity waves and entropy waves for Mach 15 flow over 3-D blunt leading edges. Initial transient growth of instability waves near the leading edge has been simulated using high-order finite difference method on parallel computers. "Transient growth" mechanism is used to explain and verify the results from the simulations. Additionally,

effects of spanwise wave number β, effects of $y-z$ angle φ, nonlinearity effects, wall temperature effects on the instability growth are studied in the receptivity to freestream standing vorticity waves. Effects of inhomogeneous boundary conditions or low-amplitude random distributed roughness on the surface are investigated in this paper, too.

2 Numerical Methods

The governing equations are the unsteady three-dimensional Navier-Stokes equations written in a conservation-law form

$$\frac{\partial U}{\partial t}+\frac{\partial F_j}{\partial x_j}+\frac{\partial F_{vj}}{\partial x_j}=0 \tag{1}$$

where

$$U = \{\rho,\ \rho u_1,\ \rho u_2,\ \rho u_3,\ e\} \tag{2}$$

$$F_j = \begin{Bmatrix} \rho u_j \\ \rho u_1 u_j + p\delta_{1j} \\ \rho u_2 u_j + p\delta_{2j} \\ \rho u_3 u_j + p\delta_{3j} \\ (e+p)\,u_j \end{Bmatrix} \tag{3}$$

$$F_{vj} = \begin{Bmatrix} 0 \\ \tau_{1j} \\ \tau_{2j} \\ \tau_{3j} \\ \tau_{jk}u_k - q_j \end{Bmatrix} \tag{4}$$

$$p = \rho RT \tag{5}$$

$$e = \rho(c_v T + \frac{\rho}{2}u_k u_k) \tag{6}$$

$$\tau_{ij} = -\mu\left(\frac{\partial u_i}{\partial x_j}+\frac{\partial u_j}{\partial x_i}\right)+2\mu/3\frac{\partial u_k}{\partial x_k}\delta_{ij} \tag{7}$$

$$q_j = -\kappa\frac{\partial T}{\partial x_j} \tag{8}$$

The details for the expressions above can be found in [32]. The viscosity and heat conductivity coefficients are computed by the Sutherland law and the assumption of a constant Prandtl number. Perfect gas assumption is used in all flows considered in this paper, though the method presented here can be easily extended to nonequilibrium real-gas hypersonic flows.

For numerical simulations of flow fields over a curved body surface, structured body fitted grids are used to transform the governing equations (1) in the Cartesian coordinates into a set of curvilinear three-dimensional coordinates (ξ, η, ζ, τ) along the body fitted grid lines. The transformation relations for the two set of coordinates are

$$\begin{cases} \xi = \xi(x,y,z,t) \\ \eta = \eta(x,y,z,t) \\ \zeta = \zeta(x,y,z,t) \\ \tau = t \end{cases} \Longleftrightarrow \begin{cases} x = x(\xi,\eta,\zeta,\tau) \\ y = y(\xi,\eta,\zeta,\tau) \\ y = y(\xi,\eta,\zeta,\tau) \\ t = \tau \end{cases} \tag{9}$$

The governing equations (1) are transformed as follows

$$\frac{1}{J}\frac{\partial U}{\partial \tau}+\frac{\partial E'}{\partial \xi}+\frac{\partial F'}{\partial \eta}+\frac{\partial G'}{\partial \zeta} +\frac{\partial E'_v}{\partial \xi}+\frac{\partial F'_v}{\partial \eta}+\frac{\partial G'_v}{\partial \zeta}+U\frac{\partial(\frac{1}{J})}{\partial \tau}=0 \tag{10}$$

where

$$E' = \frac{F_1\xi_x+F_2\xi_y+F_3\xi_z+U\xi_t}{J} \tag{11}$$

$$F' = \frac{F_1\eta_x+F_2\eta_y+F_3\eta_z+U\eta_t}{J} \tag{12}$$

$$G' = \frac{F_1\zeta_x+F_2\zeta_y+F_3\zeta_z+U\zeta_t}{J} \tag{13}$$

$$E'_v = \frac{F_{v1}\xi_x+F_{v2}\xi_y+F_{v3}\xi_z}{J} \tag{14}$$

$$F'_v = \frac{F_{v1}\eta_x+F_{v2}\eta_y+F_{v3}\eta_z}{J} \tag{15}$$

$$G'_v = \frac{F_{v1}\zeta_x+F_{v2}\zeta_y+F_{v3}\zeta_z}{J} \tag{16}$$

where J is the Jacobian of the coordinate transformation, and ξ_x, ξ_y, ξ_z, η_x, η_y, η_z, η_t, ζ_x, ζ_y, and ζ_z are the grid transformation matrices. In the equations, the transformed inviscid fluxes E', F', and G' are standard flux terms with known eigenvalues and eigenvectors. The transport flux terms E'_v, F'_v, and G'_v contain both first-order and second-order spatial derivatives of velocity and temperature. These derivatives in the Cartesian coordinates (x,y,z) are transformed into the computational coordinates (ξ,η,ζ) using a chain rule for spatial discretization.

In this paper, high-order semi-implicit method [33] is implemented to solve 3-D Navier-Stokes equations on parallel computers. A fifth-order upwind scheme [34] is used to discretize the inviscid flux derivatives and high-order central difference schemes are used to discretize the viscous flux terms in the equations. A simple local Lax-Friedrichs scheme is used to split the inviscid flux vectors into positive and negative wave fields. Divide and conquer (DAC) method is used to solved the big banded matrices of semi-implicit algorithms on parallel computers. Details of the method can be found in Ref. [33].

3 Results

The perturbations of an arbitrary flow variables before reaching the bow shock can be written in the following form:

$$q'_\infty = |q'|_\infty\, e^{i(\mathbf{k}_\infty\cdot\vec{x}-\omega t)} \tag{17}$$

where $|q'|$ represents one of the flow variables, $|u'|$, $|v'|$, $|w'|$, $|p'|$, and $|\rho'|$, $\mathbf{k}_\infty$ is the wavenumber, and ω is the wave frequency in the freestream before reaching the shock. If ω is equal to zero, the freestream disturbances are standing waves. Three kinds of weak perturbation

waves enforced in the freestream are studied in this thesis. They are fast acoustic waves, vorticity waves and entropy waves. The freestream perturbation amplitudes satisfy the following dispersion relations:

Fast Acoustic Waves($c^*_\infty = u^*_\infty + a^*_\infty$):

$$|u'|_\infty = \epsilon \cos\psi\,, \qquad |v'|_\infty = 0\,,$$
$$|p'|_\infty = \gamma M_\infty \epsilon\,, \qquad |\rho'|_\infty = M_\infty \epsilon\,,$$
$$|w'|_\infty = \epsilon \sin\psi$$

where ϵ represents the magnitude of freestream wave amplitude. The angle ψ is the angle of freestream wave with respect to the x axis in the x-z plane, i.e., $\psi = 0^o$ corresponds to 2-D planar fast acoustic waves.

Vorticity Waves($c^*_\infty = u^*_\infty$):

$$|v'|_\infty = \epsilon \cos\varphi\,, \qquad |u'|_\infty = 0\,,$$
$$|p'|_\infty = 0\,, \qquad |\rho'|_\infty = 0\,,$$
$$|w'|_\infty = \epsilon \sin\varphi$$

where the angle φ is the angle of freestream wave with respect to the z axis in the y-z plane for vorticity waves.

Entropy Waves($c^*_\infty = u^*_\infty$):

$$|v'|_\infty = 0\,, \qquad |u'|_\infty = 0\,,$$
$$|p'|_\infty = 0\,, \qquad |\rho'|_\infty = \rho_\infty \epsilon\,,$$
$$|w'|_\infty = 0$$

The parameter k is the dimensionless freestream wave number which is related to the dimensionless circular frequency ω by:

$$\omega = k\,(\cos\psi + M_\infty^{-1}) \tag{18}$$

We also define a receptivity parameter as a ratio of maximum disturbance amplitudes inside boundary layer to the free-stream forcing wave amplitude, i.e.,

$$|A| = \frac{|q'|_{max}}{C_\infty \epsilon} \tag{19}$$

where $|q'|_{max}$ is the Fourier amplitude for a flow variable q at the location of the maximum instability amplitudes inside the boundary layer and C_∞ is the freestream sound speed. Generally, streamwise velocity u' is used for q' in this paper. The dimensionless frequency F is defined as:

$$F = \frac{\omega^* \nu^*}{U^{*2}_\infty}\,. \tag{20}$$

The flow is characterized by a free stream Mach number $M_\infty = \frac{u^*_\infty}{a^*_\infty}$, and a Reynolds number defined by

$$Re_\infty \;=\; \frac{\rho^*_\infty U^*_\infty d^*}{\mu^*_\infty} \tag{21}$$

The wall temperature is characterized by its ratio to the free-stream stagnation temperature, i.e.

$$\frac{T_w}{T_0} \;=\; \frac{T^*_w}{T^*_\infty\left(1 + \frac{\gamma-1}{2} M^*_\infty\right)} \tag{22}$$

where T^*_w and T^*_∞ are the wall temperature and the free-stream temperature respectively.

In general, a numerical simulation study for a hypersonic layer receptivity problem is carried out in three steps. First, a steady flow field is computed by advancing the flow solutions to convergence with no disturbances imposed in the free stream. Second, unsteady viscous flows are computed by imposing 3-D fast acoustic single-frequency waves, vorticity waves, or entropy waves on the steady flow variables at the free stream side of the bow shock. The unsteady simulation is nonlinear by computing the transient flow solutions of the Navier-Stokes equations without any linearization in the equations and in the shock jump conditions. The wave interaction with the shock and the development of instability wave in the boundary layer are simultaneously resolved by the simulation. For traveling waves, the unsteady calculations are carried out for about 20 to 40 temporal periods until the solutions reach a periodic state in time. For standing waves, the unsteady calculations are carried out until it reaches steady state. Third, a fast Fourier transform (FFT) is performed on the perturbation variables to obtain the Fourier amplitudes and phase angles of the perturbations of the unsteady flow variables throughout the flow field. For traveling waves, the unsteady computations are carried out for one additional period in time to record the perturbations with respect to the steady flow field obtained previously. For standing waves, FFT analysis is only performed spatially. The shock/disturbance interactions and generation of T-S waves in the boundary layer are solved using the nonlinear Rankine-Hugoniot relations at the shock and the full Navier-Stokes equations in the flow fields.

3.1 Steady Mean Flow

The body surface of a 3-D parabolic leading edge is given by

$$x^* = b^* {y^*}^2 - d^* \tag{23}$$

where b^* is a given constant and d^* taken as the reference length. The body surface is assumed to be a non-slip wall with an isothermal wall temperature T^*_w.

The specific flow conditions are

$$M_\infty = 15 \qquad \epsilon = 1 \times 10^{-4}$$
$$T^*_\infty = 192.989\,K \qquad p^*_\infty = 10.3\,Pa$$
$$T^*_w = 1000\,K \qquad \gamma = 1.4$$
$$R^* = 286.94\,Nm/kgK \qquad Pr = 0.72$$
$$T^*_r = 288\,K \qquad T^*_s = 110.33\,K$$
$$\mu^* = 0.17894 \times 10^{-4} kg/ms\,.$$
$$b^* = 4\,m^{-1} \qquad d^* = 1.0\,m$$
$$\text{Nose Radius of Curvature} = r^* = 0.125\,m$$
$$Re_\infty = \rho^*_\infty U^*_\infty d^*/\mu^*_\infty = 60265.5$$

There is no flow in spanwise direction.

Figure 3 shows the steady solution of streamwise velocity contours by a set of $281 \times 121 \times 4$ computational grids obtained by using 4 processors simultaneously and pressure distributions along wall-normal direction respectively. Edges in figure are the boundaries of subdomains. The i indices of the grid lines in the figures are between 1 and 151, where $i = 1$ is located at the stagnation line. The x_s coordinates of the grid-line intersecting points on the body surface are listed in Table 1. In this table, x_s has been nondimensionalized by reference length d^*.

Table 1: Horizontal Coordinates of Grid Points on Surface.

Index i	x_s
1	-1.000000
40	-0.97172
70	-0.90741
110	-0.74739
140	-0.55316
160	-0.37954

The figure shows that the steady flow over the parabola for both cases develops a favorable pressure gradient which is stable to T-S waves along the body surface. The magnitudes of the negative pressure gradients on the body surface decrease as the flow moves downstream. Due to the effects of nose bluntness, the pressure has a slight variation across the boundary layer in the region near the leading edge. The pressure distribution across the boundary layer approaches a constant as the flow develops further downstream.

3.2 Receptivity to Fast Acoustic Waves

The generation of boundary-layer T-S and inviscid instability waves by freestream fast acoustic disturbances for hypersonic flow over 3-D parabolic leading edge has been firstly simulated. A number of computational cases are studied on the effects of frequency, and the effects of the freestream disturbance wave angle, ψ, on the hypersonic receptivity process. In this paper, results of fixed wavenumber k of fast acoustic disturbances (Case K_a) are presented while the wave angle ψ changes from 0^o to 15^o, 30^o, 45^o, 60^o, and 75^o. Parameters of different computational cases can be found in Table 2.

Figure 4 shows the instantaneous perturbation velocity, u', and Figure 5 shows the Fourier amplitude $|u'|$ contours for the single $\psi = 45^o$ oblique wave case at $F = 1815.75$ after the flow field has reached a periodic state. The instantaneous contours and the Fourier amplitude contours show that the waves inside the boundary layer near the surface are dominantly boundary layer instability waves, while the waves immediately behind the bow shock are mainly external forcing waves.

Table 2: Disturbance Parameters for Case K_a

Case #	Wave Number k	F
K_a1	141.4213	2503
K_a2	141.4213	2423.1
K_a3	141.4213	2188.67
K_a4	141.4213	1815.75
K_a5	141.4213	1329.75
K_a6	141.4213	763.791

There is an instability growth near the leading edge inside the boundary layer near the wall surface, followed by a rapid decay. These instability waves generated inside the boundary layer are actually the first mode instability waves as discussed in Ref. [35]. However, no second mode instability waves observed in Ref. [35] which has smaller amplitude than the first mode instability waves can be observed in this computational domain. Figure 6 shows the distributions of and $|u'|$ along x axis at different wall-normal location and comparison of the receptivity parameter $|u'|_{max}/\epsilon C_\infty$ of the first mode for different wave angle ψ. Along with j increasing, the values of $|u'|$ at each wall-normal location are firstly increased within the boundary layer near the surface, then gradually decreased outside the boundary layer. The maximum $|u'|$ occurs in the first mode region inside the boundary layer. So in this case, the receptivity parameter is defined as a ratio of maximum disturbance amplitudes $|u'|$ in the first mode regions to the amplitude of free-stream forcing wave, $|u'|_{max}/(\epsilon C_\infty)$. The largest receptivity parameter of the first mode happens around wave angle $\psi = 45^o$. However, the order of magnitude of the maximum amplitude of the receptivity parameter is around 1.0 for the receptivity to fast acoustic waves. It shows that the growth inside the boundary layer of the receptivity to fast acoustic waves is comparable to the amplitude of freestream disturbances.

3.3 Receptivity to Vorticity Waves

We then perform simulations of receptivities to streamwise vorticity waves and traveling vorticity waves in Mach 15 flow over a parabola blunt body respectively. Spanwise wave number effects, $y - z$ angle φ effects, nonlinearity effects, wall temperature effects and surface roughness effects are parametricly studied in the following.

3.3.1 Receptivity to Streamwise Vorticity Waves

According to Ref. [28], a streamwise-oriented vortex and zero frequency disturbances can generate stronger growth of disturbances in the boundary layer than other unsteady disturbances. In order to verify the conclusions from transient growth theory and obtain stronger

growth inside boundary layer near the leading edge, we are studying the cases of receptivity to streamwise vorticity waves in Mach 15 boundary layer over a blunt leading edge firstly.

For streamwise vorticity waves, in the freestream, nonzero disturbances are normal and spanwise velocity disturbances(v' and w') as well as the wavenumbers in wall-normal direction (k_y) and in spanwise direction (k_z). Amplitudes of other disturbances are zero. Nondimensional spanwise wavenumber β is defined as following.

$$\beta = k_z \frac{x_l}{\sqrt{Re_l}} \tag{24}$$

where x_l is reference length set to $0.685735m$ and Re_l is the Reynolds number base on x_l, which is 48447.2643 in our flow conditions. We are performing parametric studies on the cases with different nondimensional spanwise wavenumber β.

Wave Structures

Figure 7 shows the 3-D instantaneous streamwise velocity contours at spanwise wavenumber $\beta = 0.18$ and $\epsilon = 1 \times 10^{-4}$. The figure shows that after freestream streamwise vorticity waves entering the computational domain, one kind of disturbance gradually grows to further downstream inside the boundary layer near the leading edge. The amplitude of the growing disturbances is much larger than the entering freestream disturbances outside the boundary layer. Figure 8 shows the two-dimensional instantaneous u' and Fourier amplitude $|u'|$ contours at one cross section in spanwise direction of the flow field. From both figures, we can clearly observe the strong growth of the disturbances inside the boundary layer. It also shows that the waves inside the boundary layer near the surface are dominantly boundary layer instability waves, while the waves immediately behind the bow shock are mainly external forcing waves.

Figure 9 shows the streamwise vorticity, ω_x, contours at different streamwise locations: $i = 70$, $i = 110$, and $i = 140$, where the corresponding coordinates in streamwise direction can be found in Table 1. Here, the streamwise vorticity is the gradients of normal and spanwise velocity. Along with the changing of locations in downstreams, pairs of counter-rotating vortices are observed in flow field. The pair of vortices after the shock is the disturbances enforced into the flow field. There are two more pairs of counter-rotating vortices generated inside the boundary layer after the flow field has reached a periodic state. This indicates that the disturbances generated inside the boundary layer is a Görtler-like disturbances [16]. Fourier amplitude $|u'|$ distributions in wall normal direction across the boundary layer are shown in Figure 10 at the different streamwise locations $i = 80$, 120, and 150. There are two parts of initial growth inside boundary layer for this case. This can be clearly observed especially at lower spanwise wavenumbers β. For the cases with large spanwise wavenumbers β, the region of the first part of the growth are very small. In Figure 10, the shape of $|u'|$ for $\beta = 0.01$ and the shapes of $|u'|$ for $\beta = 0.08$ and 0.18 are quite different at location $i = 80$, which is the region of first part of the growth for $\beta = 0.01$ and the region of the second part of the growth for $\beta = 0.08$ and 0.18. And the amplitude of the growth for $\beta = 0.01$ is larger than that for $\beta = 0.08$ and smaller than that for $\beta = 0.18$. However, at the locations downstream, the shape of $|u'|$ for $\beta = 0.01$ gradually changes to the similar structure as the shapes for $\beta = 0.08$ and 0.18. Meanwhile, the amplitude of the growth for $\beta = 0.01$ becomes much smaller at location $i = 80$ and the amplitude of the growth for $\beta = 0.08$ becomes about the same as $\beta = 0.18$ case. At locations $i = 120$, and 150, the second growth is the dominant growth inside the boundary layer.

Since the parallel assumption is not valid near the leading-edge, we have to perform necessary linear stability (LST) analysis at the later zone to try to discover what specific unstable mode or modes cause such large amplifications and whether this growth is due to the combination effect of all stable modes. In the normal mode analysis for the linear disturbances, the fluctuations of flow quantities are assumed to be represented by harmonic waves of the following form:

$$[u', v', p', T', w']^T = \left[\hat{u}(y), \hat{v}(y), \hat{p}(y), \hat{T}(y), \hat{w}(y)\right]^T e^{i(\alpha x + \beta z - \omega t)} \tag{25}$$

where α and β are the wavenumbers in x and z directions respectively, and ω is the frequency of the disturbance waves. In our studies of receptivity to streamwise vorticity waves, ω is zero. These parameters are in general complex numbers. The complex amplitude (eigen) function of a typical flow variable is $\hat{u}(y)$. In order to compare with the DNS results, spatially stability problem is solved. In a spatial stability problem, real-valued β are assumed. While α is the complex eigenvalue to be solved for. The real part of α, α_r, represents the spatial frequency of the disturbance modes, while the imaginary part, α_i, represents the spatial amplification rate of the disturbances. When $-\alpha_i$ is greater, equal to, or smaller than zero, a disturbance mode is unstable with finite amplification, neutrally stable, or stable with finite damping, respectively. Figure 11 shows the eigen value trees from LST analysis for different β at location $i = 50$ in zone2 by using two sets of grids, 50 grid points and 100 grid points. Since ω is zero for standing waves, the eigen value trees are symmetric about zero. If there is any specific mode causing the large growth inside boundary layer, we should identify it for LST analysis. And this mode if exists is expected to be an unstable mode whose imaginary part, α_i should be negative. In this case, we can not find any unstable mode. However, there are a lot of stable modes ex-

ists. After taking closer views on the eigen value trees in Figure 11, we also found several modes at $\alpha_r = 0$ location. Even they are all very stable modes, we want to check the eigen functions of these modes and try to compare them with DNS results. We picked up three of these modes in Figure 11 and graphed the corresponding eigen functions in Figure 12. Figure 12 shows the normalized eigen functions of u_r, v_r and w_i of these picked three modes. They are normalized by eigen functions of pressure p. From these plots, we can find these modes are real modes and all of them are Görtler-like modes. However, none of them has the similar structure as we observed in Figure 10. We can not identify an specific mode causing the instability growth inside boundary layer for the case of receptivity to streamwise vorticity waves. We then try to explain this phenomena by using the "transient growth" mechanism [24]. Because the linearized Navier-Stokes equations are not self adjoint and therefore have nonorthogonal eigenmodes. There exists a coupling of oblique T-S and Squire modes in the flow field. Thus, even when all the eigenmodes are damped, some transient period of algebraic growth occurs prior to the eventual exponential decay of the disturbances. From "transient growth" mechanism, it consists of a decaying v', w' disturbance - a streamwise vortex- that moves fluid from the high-velocity region of a boundary layer to the low-velocity, near-wall region and simultaneously moves the low-velocity fluid away from the wall into the upper region. Even though the streamwise vortices decay finally, their existence continues to redistribute fluid throughout the shear layer, adding to the kinetic energy of the streamwise velocity disturbance, u'. Because the u' in the boundary layer are so much larger than the original v', w' disturbance, the kinetic energy loss associated with the decay of the streamwise vortex is negligible with respect to the disturbance kinetic energy gained by the redistribution of u'. This process is what Landahl described as the "lift-up" mechanism [22].

Streamwise Wavenumber β Effects

To study the effects of the spanwise wavenumber β on the receptivity and initial transient growth of current case near the leading edge, we performed parametric studies on the receptivity of streamwise vorticity waves at $\epsilon = 1 \times 10^{-4}$ by changing the values of β. Figure 13 shows the comparison of the variation of the $|u'_{max}|$ distributions along streamwise direction for different spanwise wavenumbers β. As β decreases from 0.24 to 0.02, the $|u'|$ amplitude approaches the largest value at $\beta = 0.18$ and decreases thereafter , meanwhile, their locations move downstream and the instability regions are extended to much longer ranges. It also clearly illustrates that before this large growth happens, there is one more small growth occurring very close to the stagnation line and then damping very quickly following a much larger growth occurs downstream.

Figure 14 shows the comparison of the receptivity parameters $|u'|_{max}/\epsilon C_\infty$ of various receptivity cases and the locations of the maximum receptivity parameters to the stagnation point for different spanwise wavenumbers β. The largest receptivity parameter is at $\beta = 0.18$ and gradually decreases along with either increasing β or decreasing β. This agrees with the results from Ref. [36] which studied the transient growth in compressible flat plate boundary layer flow. Along with spanwise wavenumbers β increasing, the locations of the the maximum amplitudes move closer to the stagnation point. To quantify the magnitudes of the instability growth inside the boundary layer, we also check the ratio of the $|u'|_{max}$ to the lowest amplitude before the instability growth. The lowest amplitude occurs at the switch points of those two parts of growth near the leading edge which are discussed in previous part. The ratios are listed in Table 3.

Table 3: Amplification Parameters for Different β

β	$\frac{\lvert u'_{max}\rvert}{\lvert u'_{min}\rvert}$	β	$\frac{\lvert u'_{max}\rvert}{\lvert u'_{min}\rvert}$
0.02	325.3	0.14	949.4
0.04	388.2	0.16	1158.37
0.06	437.7	0.18	1629.88
0.08	494.3	0.2	1352.21
0.1	524.65	0.22	1097.3
0.12	610.49	0.24	923.5

$y - z$ Angle φ Effects

Since our enforcing disturbances are 3-D disturbances in free-stream, we need consider the effects of angle φ on the receptivity to streamwise vorticity wave. Here, the angle φ is the angle of freestream wave with respect to the z axis in the y-z plane for vorticity waves. When φ is 0^o, the streamwise vorticity waves are only in spanwise direction. When φ is not zero, the disturbances has the motion in wall-normal direction. It is necessary to study the difference among the cases with different angle φ, and how the angle φ affects on the initial transient near the leading edge. In this paper, three different angles φ are chosen to make the comparisons. The spanwise wavenumber β is fixed to $\epsilon = 1 \times 10^{-4}$ for all the cases. The disturbance parameters are listed in Table 4.

Figure 15 shows the comparisons of the maximum $|u'|$ distributions along x inside boundary layer for disturbances with different $y - z$ angles φ. We can observe the intial instability growth inside the boundary layers for all the cases. Among these cases, the case with $\varphi = 0^o$ has the largest amplitudes. For non-zero φ cases, the $|u'|$ distributions along x have slight oscillations due to the up and down of the disturbances

Table 4: Disturbance Parameters for Different φ

φ	k	k_y	β
0^o	57.7764	0.0	0.18
30^o	66.7145	33.3572	0.18
45^o	81.7082	57.7764	0.18
60^o	115.553	100.0717	0.18

in wall-normal direction. The amplitude of $\varphi = 60^o$ is larger than that of $\varphi = 30^o$ and $\varphi = 45^o$ at the region very close to the stagnation point. However, the case with $\varphi = 30^o$ approaches larger amplitudes than other two downstream. This is because that the $\varphi = 60^o$ case has larger k_y in wall-normal direction. This will cause the freestream disturbances move back and forth much faster than $\varphi = 30^o$ and $\varphi = 45^o$ cases. This kind of back and forth of the disturbances will accumulate the disturbances at the region near the stagnation point.

Since $\varphi = 0^o$ has the largest instability growth inside the boundary layer near the surface, our next computations will focus on the cases with $y - z$ angle $\varphi = 0^o$.

Nonlinearity Effects

For weak monochromatic free stream forcing waves, the generation of boundary-layer instability waves with the same fundamental frequency are expected to be linear with respect to the forcing amplitudes. However, nonlinearity phenomena will be observed if we keep increasing the amplitudes of the freestream disturbances, ϵ. To study the nonlinearity effects on the receptivity to freestream streamwise vorticity waves, we computed different cases by increasing the amplitudes of the freestream disturbances ϵ from 1×10^{-4} to 1×10^{-1}. Figure 16 shows the maximum $|u'|$ amplitudes as functions of disturbance amplitudes of the free stream forcing waves $\beta = 0.18$. The dotted lines are the expected linear response to the free stream forcing amplitudes. The figure shows that when ϵ is very small, the receptivity of the wave mode of the fundamental frequency is linear. As ϵ increases, the receptivity results deviate from the linear curves due to the nonlinear interactions.

As the forcing amplitudes increase, the nonlinear effects become significant. The nonlinear effects are a results of nonlinear interaction among the wave modes and their superharmonics. Figure 16 also shows the scaled Fourier amplitudes $|T'|/\epsilon$ along a parallel grid line near the body surface for two cases of different values of ϵ at $F = 2655$. The fundamental mode ($n = 1$), second harmonic ($n = 2$), and mode 3 ($n = 3$) for both cases are plotted in the figure. The scaled amplitudes of the two cases should be the same for linear modes. The figure shows that receptivity of the fundamental modes are governed by a linear mechanism, while the second harmonic and mode 3 are nonlinear with respect to ϵ.

Wall Temperature Effects

It has been shown using linear stability analysis that wall cooling stabilizes the first mode but destabilizes the second mode in a hypersonic boundary layer over a flat plate. In this part, the wall-cooling effect as well as adiabatic wall effect on the hypersonic leading-edge receptivity is studied by comparing the receptivity to the streamwise vorticity waves at $\beta = 0.18$ and $\epsilon = 1 \times 10^{-4}$ for isothermal wall boundary conditions with different wall temperatures and adiabatic wall boundary conditions. For the cases of isothermal wall, all cases have relatively cold walls with respect to the free-stream total temperature, $T_w/T_0 = 0.1126$ ($T_w = 1000K$), 0.0901 ($T_w = 800K$), and 0.0563 ($T_w = 500K$) respectively. For the case of adiabatic wall, the wall temperature varies in 8000-9000K, which has T_w/T_0 around 1. All other non-dimensional parameters of these cases, M_∞, Re_∞, γ, and Pr are the same.

Figure 17 shows wall-normal temperature distributions at different streamwise locations for the case with isothermal wall and the case with adiabatic wall. For both cases, the temperature increases gradually from shock to the region of boundary layer. Due to the effect of viscous dissipation and heating conduction on the temperature field in the boundary layer, the temperature approaches a peak value and then decreases due to the wall-cooling effect for the case with isothermal wall. However, for the adiabatic wall, on the contrary, the amplitude of temperature keeps increasing and approaches the peaks value on the surface. So for the case with isothermal wall, there is a large temperature gradient on the body surface due to the fact that the wall temperature is low compared to the free-stream total temperature T_0. And for the case with adiabatic wall, the temperature gradually increases from the location right after the shock to wall surface and the temperature on the surface has the largest value compared to that in the flow field. Figure 18 shows $|u'|_{max}$ and $|s'|_{max}$ distributions along x with different wall temperatures conditions. It is shown that the growth for the cases with isothermal walls is much larger than the case with adiabatic wall. Among isothermal wall cases, the lower the temperature on the surface, the larger the maximum $|u'|$ and $|s'|$ inside the boundary layer. This agrees with the results from Ref. [24] which performed studies on flat plate flow. Figure 18 implies that the higher wall temperature will destabilize the first part of the growth and stablize the second part of the growth.

3.3.2 Receptivity to Traveling Vorticity Waves

In this part, we introduce traveling vorticity waves instead of standing vorticity waves ($\omega = 0$) in the free stream and perform studies on hypersonic boundary layer receptivities to traveling vorticity waves. We

fix the spanwise wavenumber β to 0.18 which is the wavenumber that the largest instability growth can be observed inside boundary layer for standing vorticity wave in the free stream at current flow conditions. The streamwise frequency ω is nondimensionalized by,

$$\omega = \omega^* x_{ref}/u_{ref} \tag{26}$$

where x_{ref} is the reference length set to $0.55m$ and reference velocity is set to the velocity right after the shock at this location, which is $2913.033m/s$. Three different kinds of ω are considered in this part. They are $\omega = 10$, 20, and 30.

Figure 19 shows the $|u'|$ contours for the case with $\omega = 30$ at $\beta = 0.18$ and $\epsilon = 1 \times 10^{-4}$. Figure 20 shows comparisons of the maximum $|u'|$ distributions along x axis for above three cases and $\omega = 0$ case and the Fourier amplitude $|u'|$ distributions in wall-normal direction for all cases at location $i = 110$. The structure of Fourier amplitude $|u'|$ distributions in wall-normal direction looks similar for all cases. The the case with $\omega = 0$ has the largest initial growth near the leading edge among all the cases. This agrees with the conclusions from "transient growth" theory [24]. But the wave structures inside boundary layer for all non-zero ω cases are more complicated than that for the case with $\omega = 0$. For instance, at $\omega = 30$, there are three parts of growth can be observed and the largest one is the second peak. It is also shown that larger instability growth is generated along with ω increasing.

3.3.3 Surface Roughness Effect

We then continue our studies on the effects from the surface roughness on the instability growth inside the boundary layer near the leading edge. Two types of surface roughness modelings are introduced in our numerical simulations. The first one is a parametric study of inhomogeneous boundary condition on the surface. The second one is derived from considerations of asymptotic equations at high Reynolds numbers under assumption of small height of the humps [37].

Inhomogeneous Velocities on the Surface

For the first type of surface roughness modelings, we are using inhomogeneous wall-normal direction velocity boundary condition on the surface. We also enforce the mass conservation conditions on it. The inhomogeneous small velocities are randomly distributed along the surface and their amplitudes are governed by parameter ϵ_n. On the wall, non-slip velocity conditions becomes to:

$$\begin{aligned} u\ |_{wall} &= \epsilon_n f(x,z) V_n \sin\theta \\ v\ |_{wall} &= \epsilon_n f(x,z) V_n \cos\theta \end{aligned} \tag{27}$$

where ϵ_n is the amplitude parameter for inhomogeneous velocities V_n on the surface, $f(x,z)$ is the random function between (-1,1), and θ is the angle of the normal direction of the surface with respect to the y axis. $\sum f(x,z) = 0$ is also set to enforce mass conservation conditions. Different values of ϵ_n are used to change the amplitudes of V_n in our simulations. Figure 21 shows the 3-D instantaneous u' contours of the case with $\epsilon_n = 0.01$ inhomogeneous velocity on the surface at spanwise wavenumber $\beta = 0.18$. Stronger instability growth can be observed for this figure due to the effects of inhomogeneous velocity on the surface. Figure 22 shows the Fourier amplitude of $|u'|$ and $|T'|$ contours at $\epsilon_n = 0.01$ and $\epsilon_n = 0.03$ respectively. The instability growth is getting stronger due to the changing of amplitudes of the inhomogeneous velocities on the surface. Figure 23 shows the comparisons of $|u'|_{max}$ distributions along x for different ϵ_n of inhomogeneous velocity strips at $\beta = 0.18$. Along with increasing of ϵ_n, the maximum $|u'|$ of the instability growth within boundary layer becomes larger. Comparing to the case without inhomogeneous velocities on surface, the maximum $|u'|$ can be increased about 20 times at $\epsilon_n = 0.12$. Figure 23 also shows the difference between two kinds of lengths of the inhomogeneous velocities strips on the surface at $\epsilon_n = 0.09$. It is shown that the longer the the region of inhomogeneous velocities on surface, the larger the growth it can approach.

Random Roughness Strips on the Surface

The second modeling of surface roughness is derived by considering asymptotic equations on the wall boundary conditions [37]. Due to these surface roughnesses, the "true" wall has the coordinates $y = \epsilon_k g(x,z)$. Then the boundary conditions on the wall are:

$$u = v = w = \frac{dp}{dy} = 0 \quad \text{at } y = \epsilon_k g(x,z) \tag{28}$$

with ϵ_k the roughness amplitude and $g(x,z)$ the roughness distribution function. Temperature boundary conditions at wall are different for isothermal wall and adiabatic wall. Here, we are focusing on the cases with isothermal wall. The roughness Reynolds number Re_k can be defined as following.

$$Re_k = \frac{\rho_e^* U_e^* \epsilon_k}{\mu_e^*} \tag{29}$$

where the variables with subscript e are the variables at the edge of boundary layer.

For small roughness amplitude we can do Taylor expansion on Eq. (28).

$$u(x, \epsilon_k, z) = u(x,0,z) + \left.\frac{\partial u}{\partial y}\right|_{y=0} \epsilon_k g(x,z) + O({\epsilon_k}^2) \tag{30}$$

and similarly for v, w and T. The computational domain in the vertical direction extends from $y = 0$, where the Robin-type boundary condition

$$u(x,0,z) + \left.\frac{\partial u}{\partial y}\right|_{y=0} \epsilon_k g(x,z) = 0 \tag{31}$$

is implicitly enforced. The boundary conditions are accurate up to $O(\epsilon_k)$. Furthermore, the inequality $\epsilon_k \leq \triangle y_{min}$ must be hold to maintain the stability requirement. Here, the $\triangle y_{min}$ is the minimum grid distance along the vertical direction.

There are mainly two types of walls considered in this paper:

- Random roughness:

$$g(x,z) = f_0(x,z) \tag{32}$$

  where $f_0(x,z)$ is the white noise function in the interval [-1,1].

- Rough Gaussian strip along z

$$g(x,z) = f_0(x,z)e^{-50(x-0.8)^2} \tag{33}$$

Since the rough Gaussian strip along z is more efficient than the distributed roughness, the results presented in this part are mainly computed by this modeling even we have done all the computational cases. We perform several computational cases by choosing different values of roughness amplitude $\epsilon_k = 0.01\mu m$, $1\mu m$, $3\mu m$ and $5\mu m$. The corresponding roughness Reynolds numbers, Re_k, at $i = 110$ are 0.0761968, 0.761968, 2.28594, and 3.8099 respectively. According to Ref. [31], it is low-amplitude roughness when Re_k is less than 15. All of our computational cases are using low-amplitude roughness on the surface.

Figure 24 shows the 3-D instantaneous u' contours of the case with surface roughness amplitude $\epsilon_k = 1\mu m$ at wavenumber $\beta = 0.18$. Due to the strong effects from surface roughness, the wave structures outside boundary layer are too small to be displayed in instantaneous u' contours. Figure 25 compares the Fourier amplitude $|u'|$ contours of the case with surface roughness amplitude $\epsilon_k = 0.1\mu m$ and that of the case with surface roughness amplitude $\epsilon_k = 1\mu m$. In both cases, the roughness strips are placed very close to the stagnation point and cover the whole computational domain to the end of the zone. Because of the presence of the surface roughness strips, strong disturbances generated from surfaces interact with the instability growth inside the boundary layer near the surface due to the receptivity process to standing vorticity wave. This results in a series of strong disturbances near the leading edge. The amplitudes of these disturbances are varying with changing of the amplitude of the surface roughness ϵ_k. When $\epsilon_k = 0.1\mu m$, the amplitudes of the new generated disturbances are comparable to the instability growth inside boundary layer. However, when ϵ_k increases to $1\mu m$, the amplitudes of the new generated disturbances are much stronger than the instability growth inside boundary layer.

Figure 26 shows the the streamwise vorticity contours with the amplitude of surface roughness $\epsilon_k = 1\mu m$. New counter-rotating vortices are generated inside the boundary layers downstream. Despite that the main structure of the instability inside boundary layer maintains the original size, some structures are generated from surface and interact with the main instability growth. Zoomed streamwise vorticity contours are shown in Figure 27. For the case of $\epsilon_k = 0.1\mu m$, the structures of counter-rotating vortices are not impacted. When the amplitude of surface roughness becomes to $3\mu m$, from Figure 27, the structure of the main counter-rotating vortices can not be maintained and was broken to more small vortices which are also counter-rotating vortices. Larger instability growth occurs in these case due to the strong effect from the surface roughness. Much strong "lift-up" phenomena occurs in these cases due to those counter-rotating vortices inside boundary layer. This agrees with the results from previous theoretical and experimental. Figure 28 shows the comparison of maximum $|u'|$ distributions and comparison of the maximum receptivity parameters $|u'|_{max}/(\epsilon C_\infty)$ for different roughness amplitude ϵ_k at $\beta = 0.18$. The amplitudes of instability growth inside boundary layer are dramatically increased by the surface roughness. When $\epsilon_k = 5\mu m$, the receptivity parameter is about 20 times larger than that of the case without surface roughness.

We then introduce traveling vorticity waves into the flow field to study the effects from the traveling waves and how surface roughness affects the instability growth inside the boundary. Same definition of the frequency ω of the traveling waves in Eq. 26 is used. We fix the value of ω to 20 and change the amplitudes of surface roughness ϵ_k. Three different cases, $\epsilon_k = 0.1\mu m$, $\epsilon_k = 1\mu m$, and $\epsilon_k = 3\mu m$ are studied at $\epsilon = 1 \times 10^{-4}$ and $\beta = 0.18$. Figure 29 shows the Fourier amplitude $|u'|$ and $|T'|$contours for the receptivity to vorticity waves with random roughness $\epsilon_k = 1\mu m$ at $\omega = 20$ and $\beta = 0.18$. Because the existences of traveling waves, the wave structures of the instabilities inside boundary layer are changed a lot compared to the case with standing vorticity waves ($\omega = 0$). From both $|u'|$ and $|T'|$ contours, we can not observe the small disturbances generated from surface roughness. Instead, a dominant growth exists because of the traveling wave. Figure 30 shows the comparisons of $|u'|_{max}$ distributions along x for different amplitudes of surface roughness with or without traveling waves with $\omega = 20$ in spanwise direction. By comparing the maximum $|u'|$ distributions along x for no surface roughness cases at $\omega = 0$ and 20, we can observe that the case using standing vorticity waves always has the largest instability growth. And small surface roughness, for instance, $\epsilon_k = 0.1\mu m$ and $1\mu m$, won't increase the growth inside the boundary layer. At larger amplitude of surface roughness, for example, $\epsilon_k = 3\mu m$, the instability growth inside the boundary layer becomes much larger than that without surface roughness. And the waves structures becomes much more complicated. This is because of the interac-

tion of these small disturbances generated from surface roughness and the traveling vorticity waves. The generated instability waves inside boundary layer have much more amplifying and damping processes.

3.4 Receptivity to Entropy Waves

From previous part and conclusions from "transient growth" theory, standing waves can produce the strongest initial growth inside boundary layer. In this part, we are paying attentions on the the cases of receptivity to streamwise entropy waves in Mach 15 boundary layer over a 3-D blunt leading edge only. For standing entropy waves in the freestream, nonzero disturbances are density disturbance(ρ') and wavenumber (k_y and k_z). Amplitudes of other disturbances are zero. We use the same nondimensional spanwise wave number β defined in previous part. Parametric studies are performed by changing the spanwise wavenumber β from 0.04 to 0.26 at $\epsilon = 1 \times 10^{-4}$.

Figure 31 shows the 3-D streamwise velocity perturbation contours at spanwise wavenumber $\beta = 0.18$. The figure shows that after freestream entropy waves enter the computational computational domain, one kind of disturbance grows inside the boundary layer near the leading edge and obtains larger amplitude in the downstream. This result is exactly the same as what we observed in the cases of receptivity to freestream streamwise vorticity waves. Figure 32 shows the Fourier amplitude $\mid u' \mid$ and $\mid T' \mid$ contours for the case of receptivity to standing entropy waves at $\beta = 0.22$. By comparing these contours with that of receptivity to streamwise vorticity waves in Figure 8, the region of the initial growth is much closer to the stagnation point. And the wave structure outside the boundary layer is different from that in the cases of receptivity to streamwise vorticity waves. Figure 33 shows the comparison of maximum $|u'|$ distributions along x for different values of spanwise wavenumber β. The larger the β, the larger the growth and the narrower the region of the growth. Among all cases, $\beta = 0.26$ has the largest amplitude of $|u'|$ inside the boundary layer. Figure 34 shows the comparisons of the receptivity parameters $|u'|_{max}/(\epsilon C_\infty)$ and the distances between the peaks of $|u'|_{max}$ to the stagnation point for different spanwise wavenumber β. From the plot, $|u'|_{max}/(\epsilon C_\infty)$ increases along with β increases while the distances between the peaks of $|u'|_{max}$ receptivity parameters and the stagnation points decreases. Along with β increasing, the value of $|u'|_{max}/(\epsilon C_\infty)$ may reach to the maximum. Moreover, it is also shown that the receptivity parameters are in the same order of magnitude as that of the cases of receptivity to streamwise vorticity waves.

4 Summary and Future work

Parametric simulations of the receptivity process to freestream fast acoustic waves, vorticity waves, and streamwise entropy waves of Mach 15 flows over 3-D blunt leading edges has been carried out in this paper. The unsteady results show that the free stream acoustic disturbances generated first mode waves in current computational domain. The first mode waves are always generated near the leading edge and are amplified before decaying rapidly. By fixing the wavenumber of the freestream disturbances, the maximum amplitude of the first mode waves occurs around wave angle $\psi = 45^o$. In simulations of the receptivity to freestream streamwise vorticity waves and entropy waves, large initial growth can be observed at the region where no unstable mode could be found by using linear stability analysis. The streamwise vorticity contours show that Görtler-like disturbances are generated inside the boundary layer near the leading edge. It has been shown that this initial growth near the leading edge can be possibly explained by the "transient growth" theory. Cooling the surface wall will strengthen the initial growth near the leading edge. By adding inhomogeneous boundary conditions or random roughness strips on the wall can strongly increase the magnitude of initial growth inside the boundary layer. Large transient growth can not be observed in the receptivity to traveling vorticity waves even with surface roughness on the surface. So far in our work, surface roughness effects are limited to low amplitude roughness strips on the wall. We will continue our work in developing good numerical modelings of larger surface roughness and study how it affects the hypersonic boundary layer stability and transition.

Acknowledgments

This work was sponsored by the Air Force Office of Scientific Research, USAF, under AFOSR Grant # F49620-00-1-0101 monitored by Dr. John Schmisseur. The views and conclusions contained herein are those of the author and should not be interpreted as necessarily representing the official policies or endorsements either expressed or implied, of the Air Force Office of Scientific Research or the U.S. Government. We also thank Dr. A. Tumin for the valuable suggestions on the modelings of surface roughness.

References

[1] Morkovin, M. V. and Reshotko, E., "Dialogue on Progress and Issues in Stability and Transition Research," *In Laminar-Turbulent Transition, IUTAM Symposium, Toulouse, France, 1989, D. Arnal, R. Michel, Editors*, Vol. Springer-Verlag Berlin, 1990.

[2] Bushnell, D., "Notes on Initial Disturbance Field for the Transition Problem," *Instability and Transition, Vol. I*, Vol. M. Y. Hussaini and R. G. Viogt, editors, pp. 217-232, Springer-Verlag, 1990.

[3] Morkovin, M., "On the Many Faces of Transition," *Viscous Drag Reduction*, C.S. Wells, editor,

Plenum 1969.

[4] Goldstein, M. E., "The evolution of Tollmien-Schlichting Waves near a Leading Edge," *Journal of Fluid Mechanics*, Vol. 127, pp. 59-81 1983.

[5] Kerschen, E. J., "Boundary-Layer Receptivity," *AIAA paper 89-1109*, 1989.

[6] Murdock, J. W., "Tollmien-Schlichting Waves Generated by Unsteady Flow over Parabolic Cylinders," *AIAA paper 81-0199*, 1981.

[7] Lin, N., Reed, H. L., and Saric, W. S., "Effect of Leading-Edge Geometry on Boundary-Layer Receptivity to Freestream Sound," *Instability, Transition, and Turbulence*, M. Y. Hussaini et al., editors, pp. 421-440, Springer-Verlag 1992.

[8] Buter, T. A. and Reed, H. L., "Boundary layer receptivity to free-stream vorticity," *Physics of Fluids*, Vol. 6, No. 10, 1994, pp. 3368–3379.

[9] Collis, S. S. and Lele, S. K., "A Computational Approach to Swept Leading-Edge Receptivity," *AIAA paper 96-0180*, 1996.

[10] Mack, L. M., "Boundary Layer Linear Stability Theory," AGARD report, No. 709, 1984.

[11] Morkovin, M. V., "Transition at Hypersonic Speeds," *ICASE Interim Report 1*, NASA CR 178315, May 1987.

[12] Arnal, D., "Laminar-Turbulent Transition Problems In Supersonic and Hypersonic Flows," *Special Course on Aerothermodynamics of Hypersonic Vehicles*, AGARD Report No. 761 1988.

[13] Reed, H. L. and Saric, W. S., "Stability of Three-Dimensional Boundary Layers," *Annual Review of Fluid Mechanics*, Vol. 21, pp. 235-284, 1989.

[14] Reshotko, E., "Hypersonic Stability and Transition," *in Hypersonic Flows for Reentry Problems, Eds. J.-A. Desideri, R. Glowinski, and J. Periaux, Springer-Verlag*, Vol. 1, 1991, pp. 18–34.

[15] Kovasznay, L. S. G., "Turbulence in Supersonic Flow," *Journal of the Aeronautical Sciences*, Vol. 20, No. 10, October 1953, pp. 657–682.

[16] Saric, W. S., "Götler Vortices," *Annual Review of Fluid Mechanics*, Vol. 26, pp. 379-409, 1994.

[17] Reed, H. L., Saric, W. S., and Arnal, D., "Linear Stability Theory Applied to Boundary Layers," *Annual Review of Fluid Mechanics*, Vol. 28, pp. 389-428 1996.

[18] Malik, M. R., "Prediction and Control of Transition in Hypersonic Boundary Layers," *AIAA Paper 87-1414*, June 1987.

[19] Lees, L. and Lin, C. C., "Investigation of the Stability of the Laminar Boundary Layer in Compressible Fluid," *NACA TN No. 1115*, 1946.

[20] Stetson, K. F. and Kimmel, R. L., "On Hypersonic Boundary Layer Stability," *AIAA paper 92-0737*, 1992.

[21] Ellingsen, T. and Palm, E., "Stability of Linear Flow," *Physics of Fluids*, Vol. 18, No. 487, March 1975.

[22] Landahl, M. T., "A note on an Algebraic Instability of Inviscid Parallel Shear Flows," *Journal of Fluid Mechanics*, Vol. 98, part 2, pp. 243-251, 1980.

[23] L. Trefethen, A. Trefethen, S. R. and Driscoll, T., "Hydrodynamic Stability without Eigenvalues," *Science*, Vol. 261, 1993.

[24] Reshotko, E., "Transient Growth: A Factor in Bypass Transition," *Physics of Fluids*, Vol 13, No. 5, pp. 1067-1075 May 2001.

[25] P. Andersson, M. B. and Henningson, D. S., "Optimal Disturbances and Bypass Transition in Boundary Layers," *Physics of Fluids*, Vol. 11, No. 1, 1999.

[26] Luchini, P., "Reynolds-Number-Independent Instability of the Boundary Layer over a Flat Surface: Optimal Perturbations," *Journal of Fluid Mechanics*, Vol. 404, 2000, pp. 289-309.

[27] Butler, K. M. and Farrell, B. F., "Three-Dimensional Optimal Perturbations in Viscous Shear Flow," *Physics of Fluid*, Vol. 4, No. 8, pp. 1637-1650, 1992.

[28] Tumin, A. and Reshotko, E., "Spatial Theory of Optimal Disturbances in Boundary Layers," *Physics of Fluids*, Vol. 13, No. 7, July 2001.

[29] M. V. Morkovin, E. R. and Herbert, T., "Transition in Open Flow Systems - A Reassessment," *Bull. Am. Phys. Soc.*, 39, 1882, 1994.

[30] S. A. Berry, S. A. Bouslog, G. J. B. and Caram, J. M., "Shuttle Orbiter Experimental Boundary-Layer Transition Results with Isolated Roughness," *Journal of Spacecraft and Rockets*, Vol. 35, No. 3, 1998, pp. 241-248.

[31] White, E. B. and Reshotko, E., "Roughness-Induced Transient Growth in a Flat-Plate Boundary Layer," *AIAA paper 2002-0138*, January 2002.

[32] Zhong, X., "Direct Numerical Simulation of Hypersonic Boundary-Layer Transition Over Blunt Leading Edges, Part I: New Numerical Methods and Validation ," AIAA paper 97-0755, Jan. 1997.

[33] Dong, H. and Zhong, X., "High-Order Semi-Implicit Schemes for Unsteady Compressible Flow Simulations," *AIAA Journal*, Vol. 40, No. 5, 2002.

[34] Zhong, X., "High-Order Finite-Difference Schemes for Numerical Simulation of Hypersonic Boundary Layer Transiton," *Journal of Computational Physics*, Vol. 144, August 1998, pp. 662-709.

[35] Zhong, X., "Leading-edge Receptivity to Free-stream Disturbance Waves for Hypersonic Flow over a Parabola," *Journal of Fluid Mechanics*, Vol. Vol. 441, pp. 315–367, 2001.

[36] A. Hanifi, P. J. S. and Henningson, D. S., "Transient Growth in Compressible Boundary Layer Flow," *Physics of Fluids*, Vol. 8, No. 3, March 1996.

[37] Bottaro, A. and Zebib, A., "Görtler Vortices Promoted by Wall Roughness," *Fluid Dynamics Research*, Vol. 19, 1997, pp. 343-362.

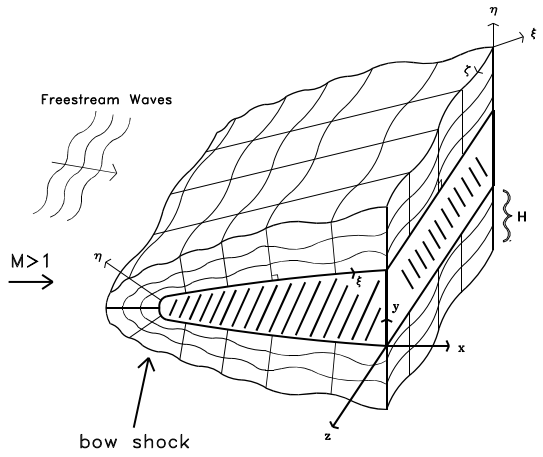

Figure 1: A schematic of 3-D shock fitted grids for the direct numerical simulation of hypersonic boundary-layer receptivity to freestream disturbances over a blunt leading edge.

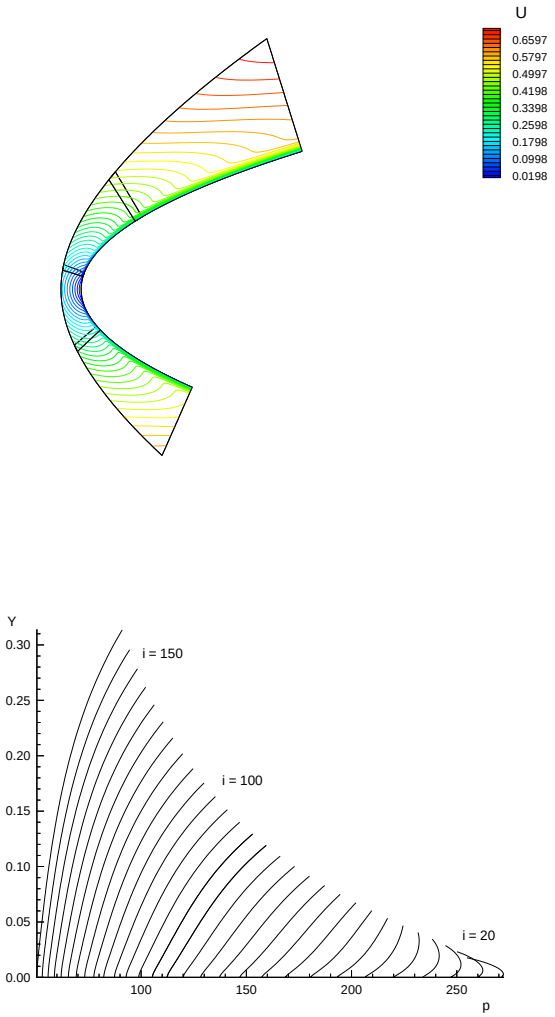

Figure 3: Streamwise velocity contours and pressure distributions along wall-normal direction.

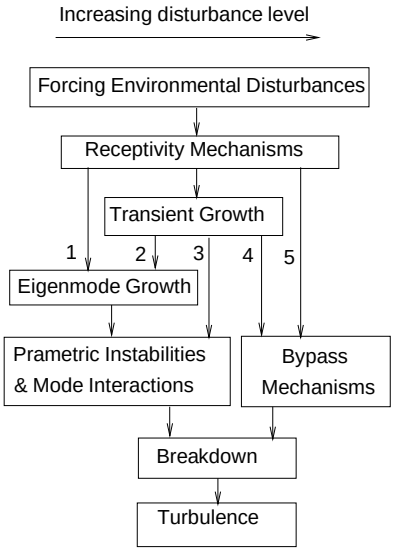

Figure 2: Paths to Turbulence in Wall Layers in Ref. [29].

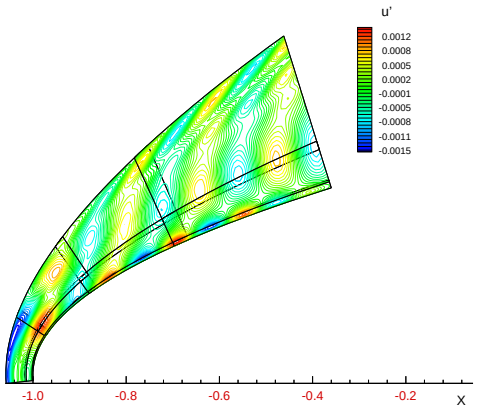

Figure 4: Instantaneous u' contours for the receptivity to oblique fast acoustic wave ($\psi = 45^o$)

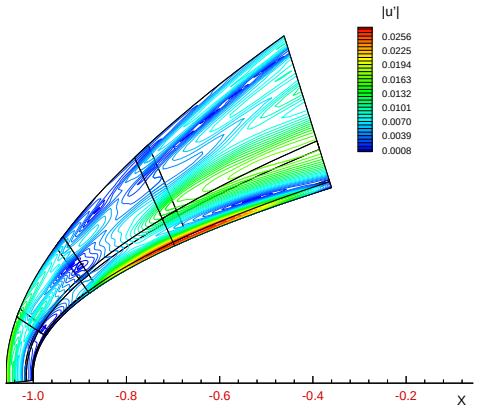

Figure 5: Fourier amplitude $|u'|$ contours for the receptivity to oblique fast acoustic wave ($\psi = 45^o$).

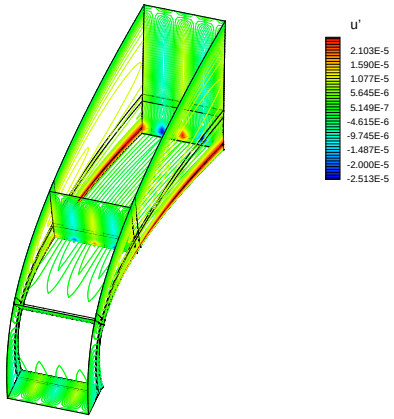

Figure 7: Three-dimensional instantaneous u' contours of receptivity to streamwise vorticity waves with wavenumber $\beta = 0.18$.

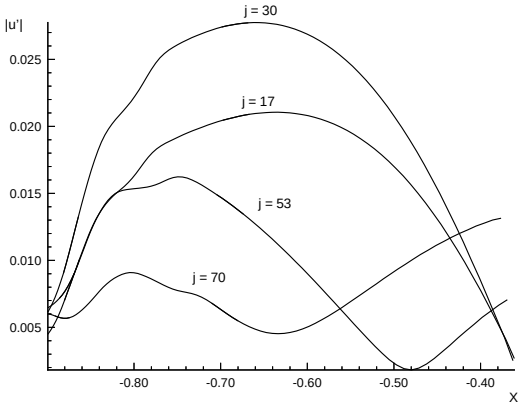

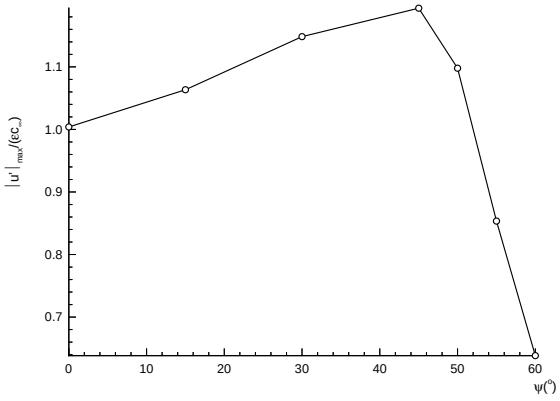

Figure 6: Distribution of and $|u'|$ at different wall-normal locations at $\psi = 45^o$ (upper figure) and comparisons of $|u'|_{max}/\epsilon C_\infty$ (lower figure) for different $x - z$ wave angles, ψ, at same wavenumber $k = 141.4213$.

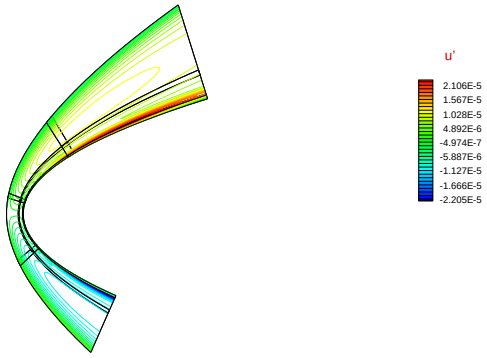

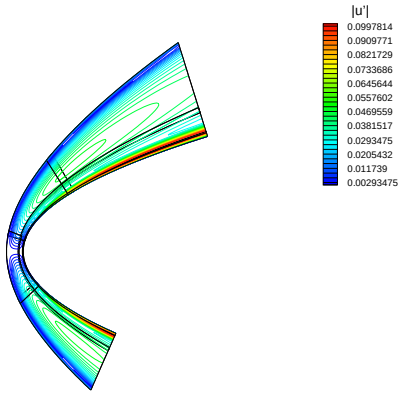

Figure 8: Instantaneous u' (upper figure) and Fourier amplitude $|u'|$ contours (lower figure) at $\beta = 0.18$.

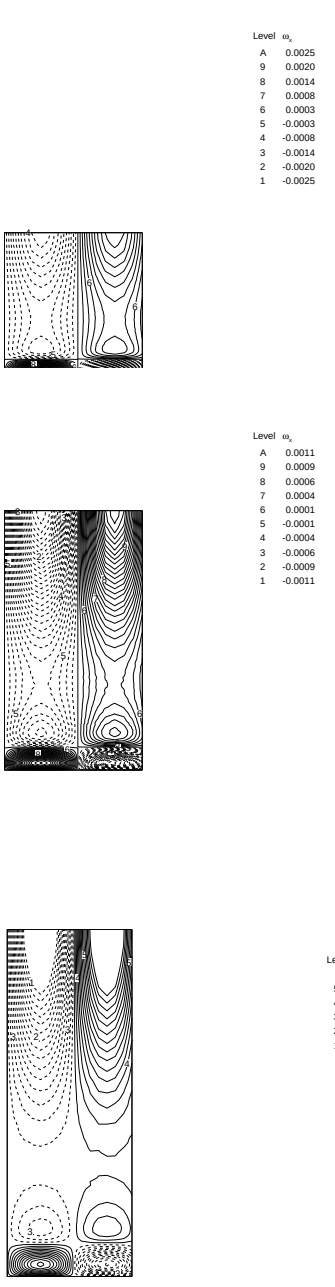

Figure 9: Streamwise vorticity, ω_x, countours at different locations in streamwise. (upper figure: $i = 70$, mid figure: $i = 110$, lower figure: $i = 140$.)

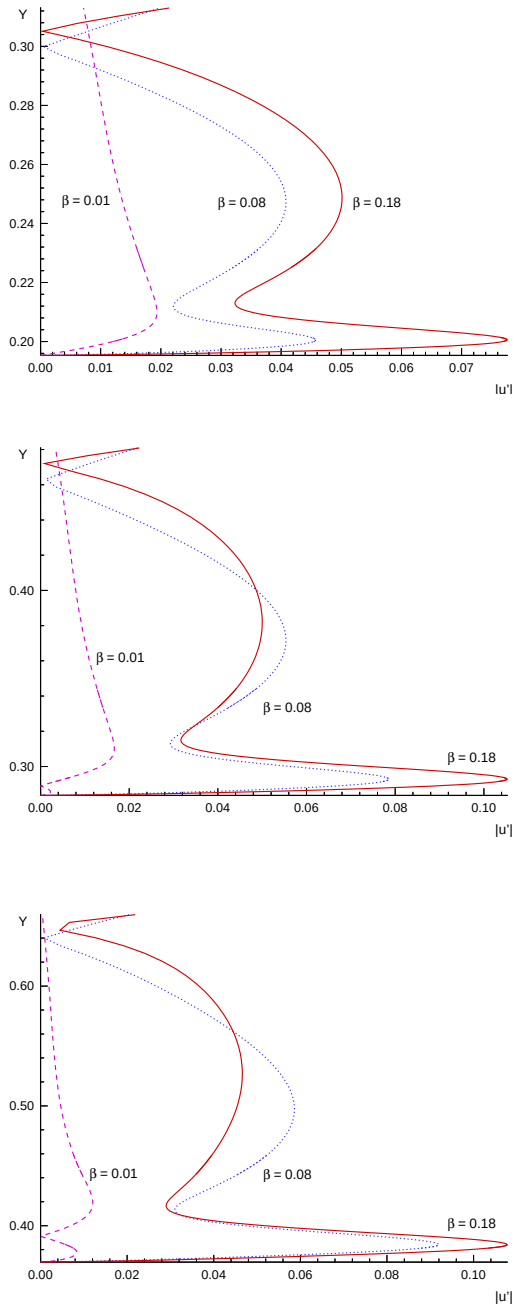

Figure 10: Comparisons of $|u'|$ along wall normal direction at different location in streamwise direction for three different wavenumber. (upper figure: $i = 80$, mid figure: $i = 120$, lower figure: $i = 150$.)

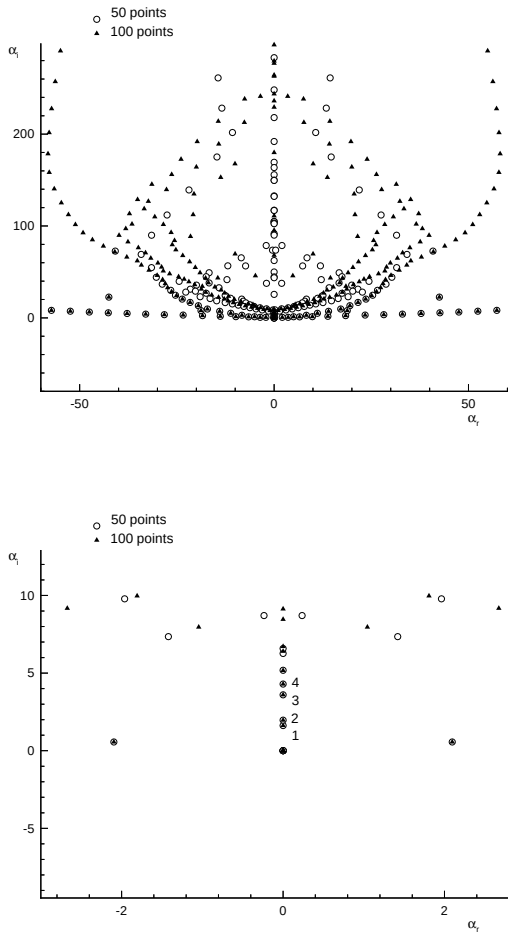

Figure 11: Eigen value trees from LST analysis for different β at location $i = 50$ in zone2.

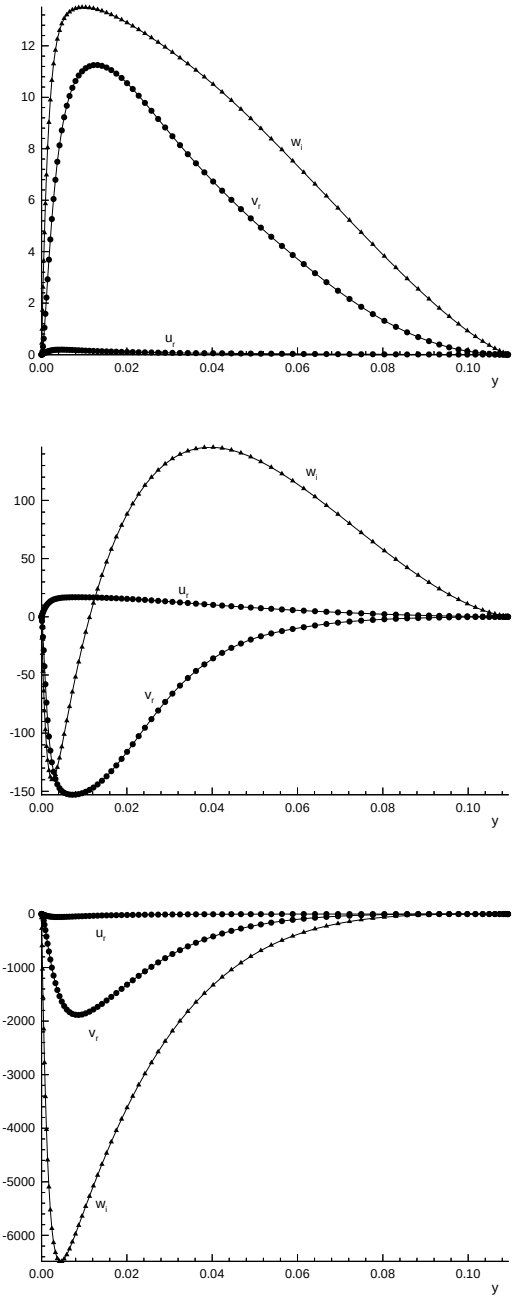

Figure 12: Eigen functions of three test modes from LST analysis for $\beta = 0.1$ at location $i = 50$ in zone2. (upper figure: mode 1, mid figure: mode 2, lower figure: mode 3.)

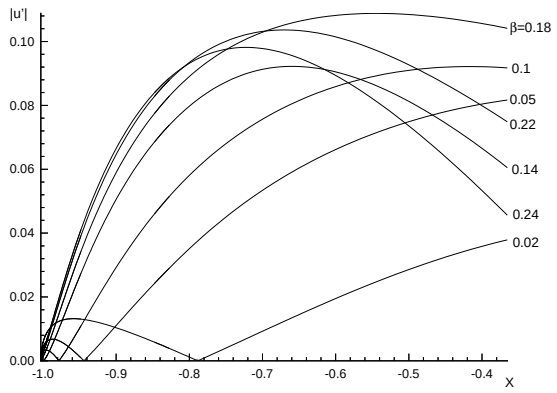

Figure 13: The variations of the Fourier amplitude $|u'|_{max}$ distributions along x for different wavenumbers, β.

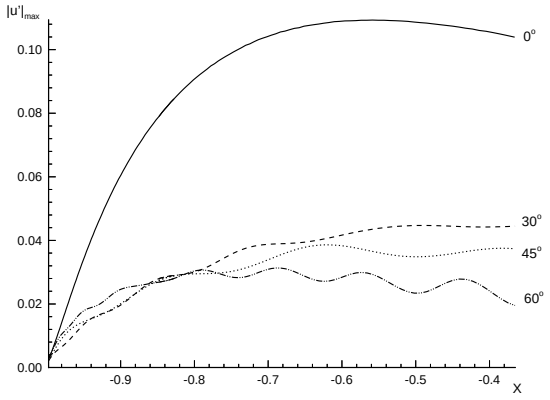

Figure 15: The variation of the $|u'|_{max}$ distributions along x near the surface for different disturbances with $y-z$ angle ϕ.

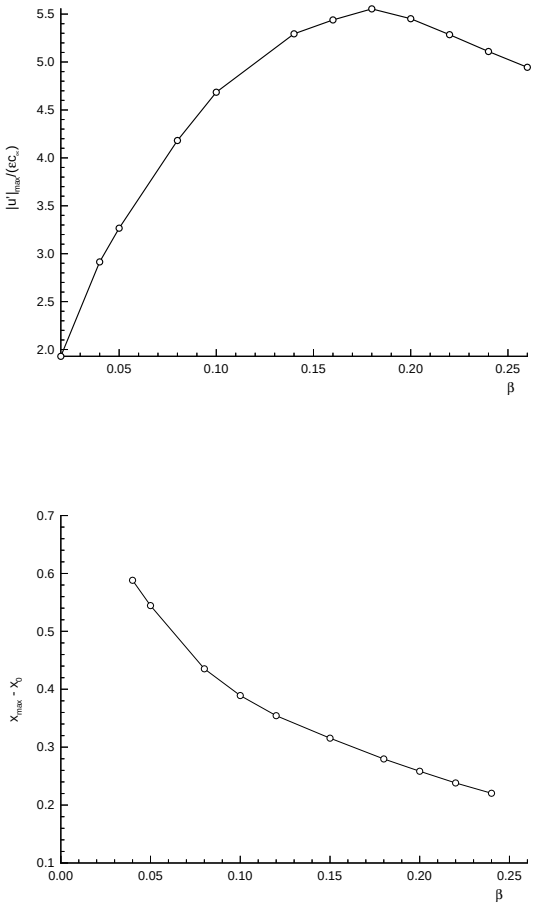

Figure 14: The variations of receptivity parameter $|u'|_{max}/\epsilon C_\infty$ (upper figure) and locations of the peak points with wavenumbers, β (lower figure).

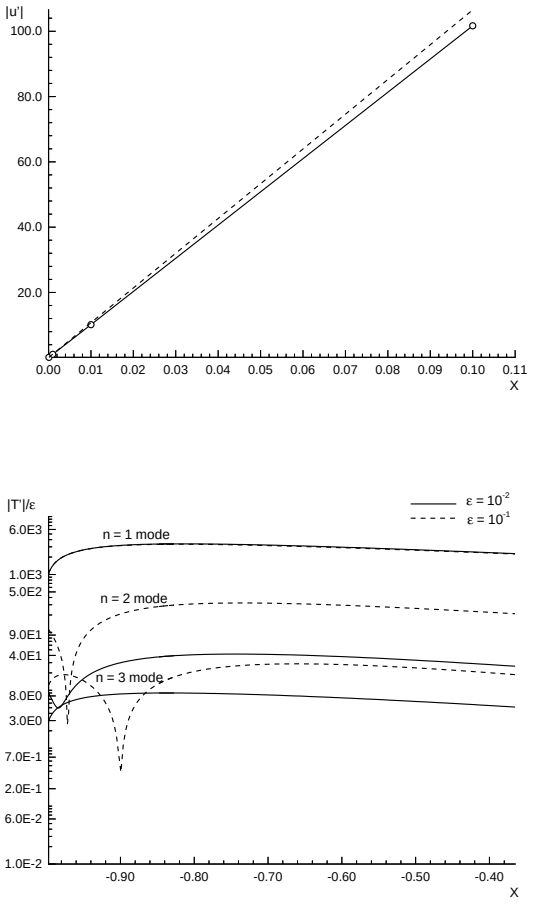

Figure 16: Fourier amplitude $|u'|_{max}$ vs. amplitudes ϵ (upper figure) and comparisons of Fourier amplitude $|u'|$ along x axis for two different amplitudes ϵ of freestream forcing disturbances (lower figure).

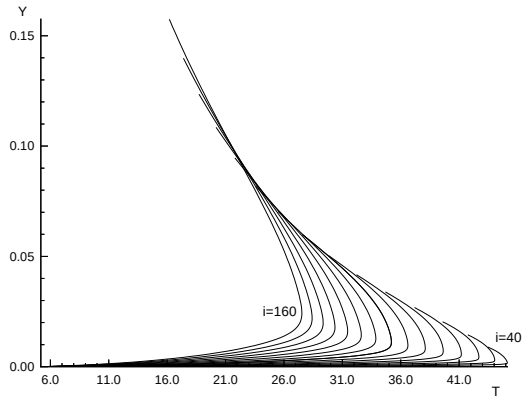

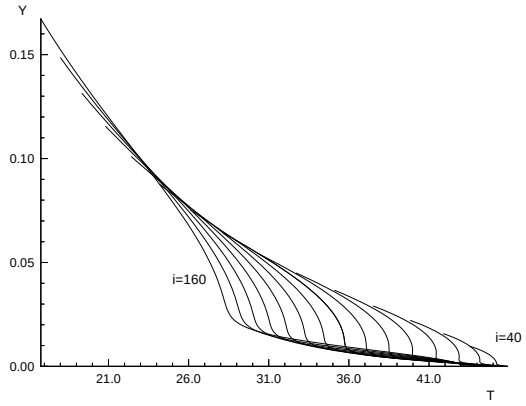

Figure 17: Temperature distributions along y direction of two different cases with isothermal wall (upper figure) and adiabatic wall (lower figure) respectively.

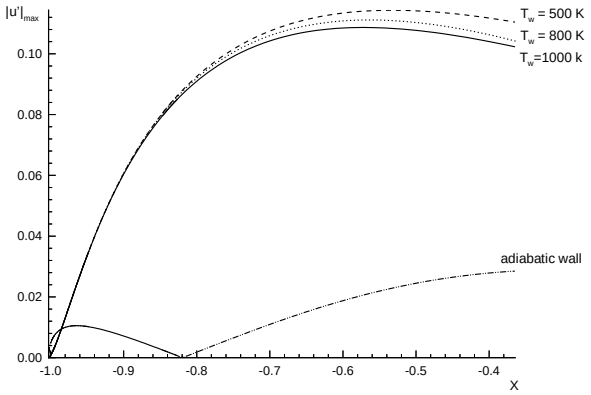

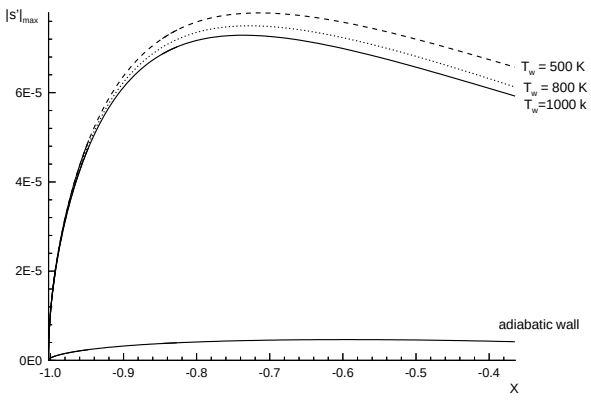

Figure 18: The variations of $|u'|_{max}$ (upper figure) and $|s'|_{max}$ (lower figure) distributions along x with different wall temperatures conditions.

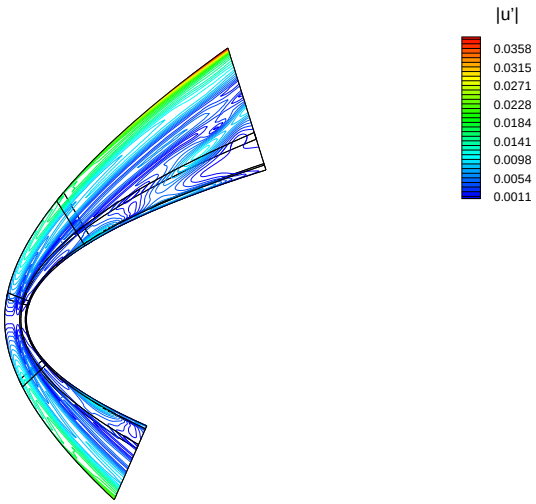

Figure 19: Fourier amplitude $|u'|$ contours for $\omega = 30$ at $\beta = 0.18$.

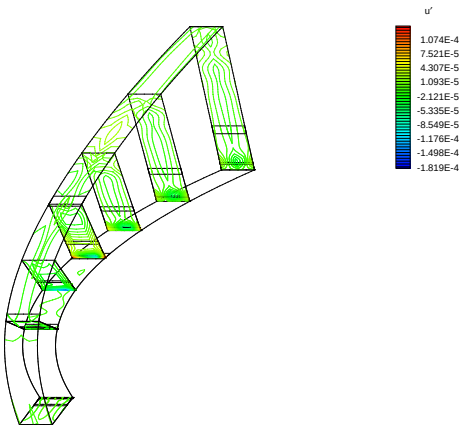

Figure 21: 3-D instantaneous u' contours of the case with inhomogeneous velocity on surface ($\epsilon_n = 0.01$) at wavenumber $\beta = 0.18$.

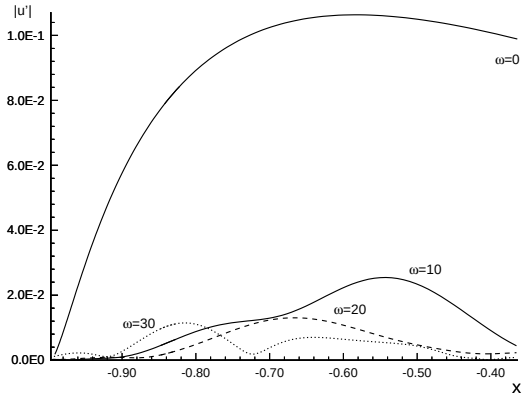

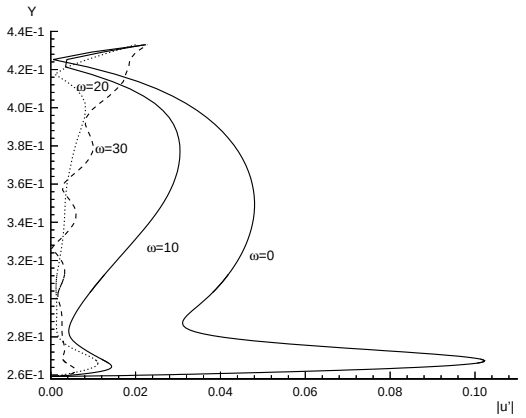

Figure 20: The variations of the $|u'|_{max}$ along x direction (upper figure) and $|u'|$ distributions along y direction at $i = 110$ (lower figure) for different frequencies, ω.

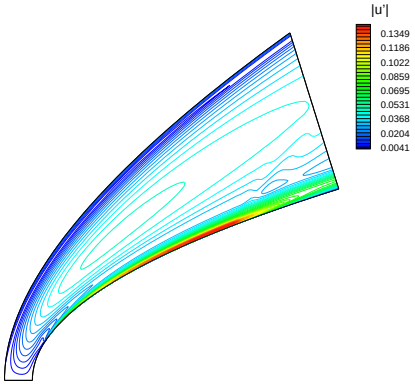

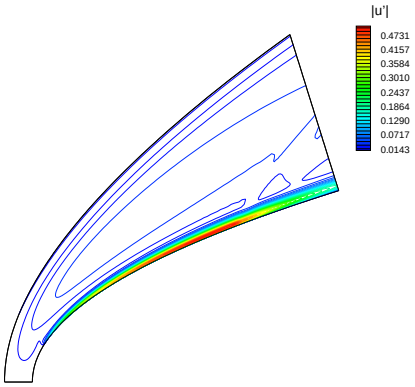

Figure 22: Fourier amplitude $|u'|$ contours for the receptivity to streamwise vorticity waves with inhomogeneous velocity on surface with $\epsilon_n = 0.01$ (upper figure) and $\epsilon_n = 0.03$ (lower figure) at $\beta = 0.18$.

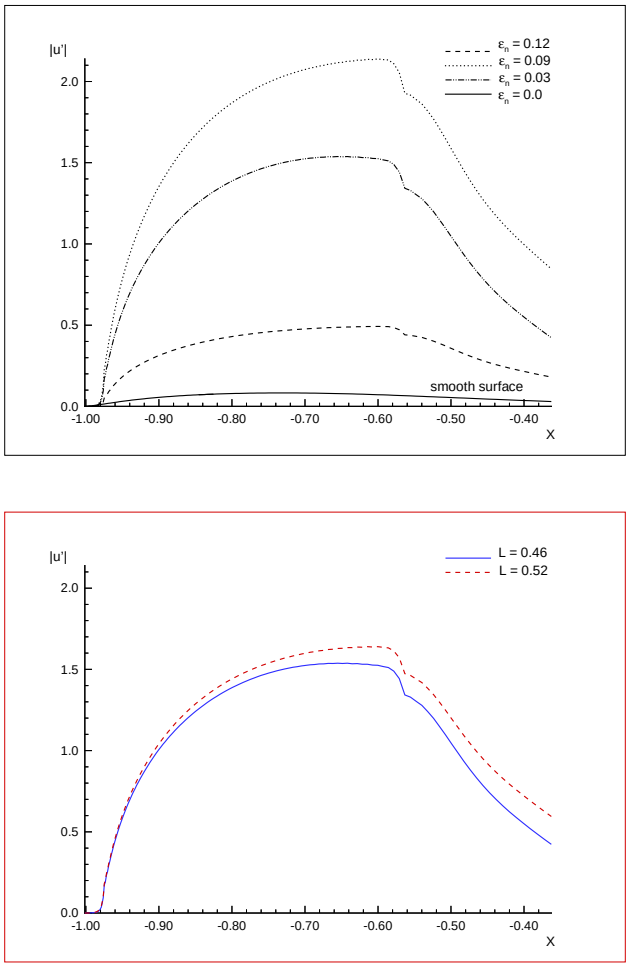

Figure 23: Comparisons of $|u'|_{max}$ (upper figure) and $|T'|_{max}$ (lower figure) for different inhomogeneous parameters and different lengths of inhomogeneous velocity strips at $\beta = 0.18$.

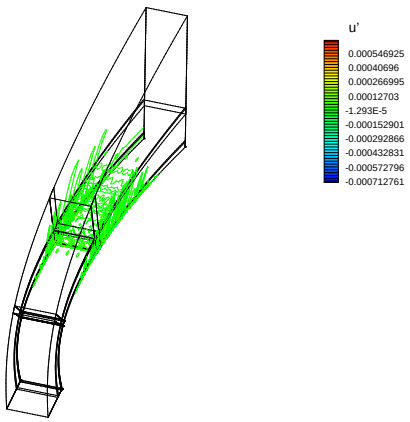

Figure 24: 3-D instantaneous u' contours of the case with random surface roughness ($\epsilon_k = 1\mu m$) at wavenumber $\beta = 0.18$.

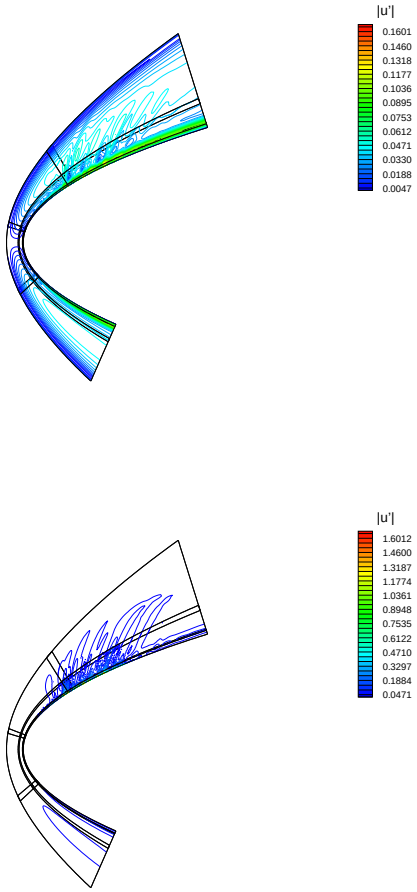

Figure 25: Fourier amplitude $|u'|$ contours for the receptivity to streamwise vorticity waves with random surface roughness at $\beta = 0.18$ with $\epsilon_k = 0.1\mu m$ (upper figure) and $\epsilon_k = 1\mu m$ (lower figure).

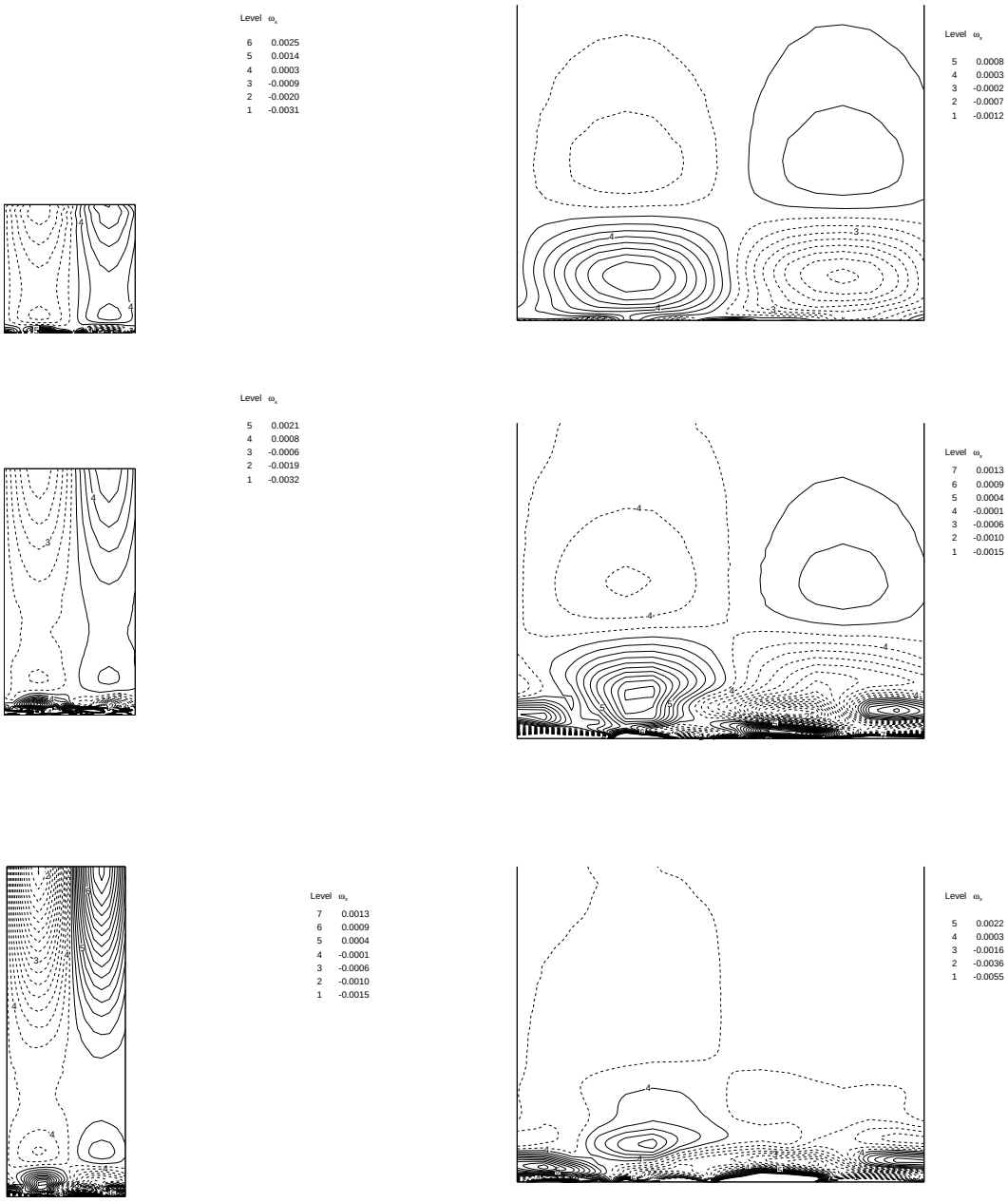

Figure 26: Streamwise vorticity, ω_x, countours at different streamwise locations for the case with random surface roughness $\epsilon_k = 1\mu m$. (upper figure: $i = 70$, mid figure: $i = 110$, lower figure: $i = 140$.)

Figure 27: Zoomed ω_x contours of the cases with surface random roughness $\epsilon = 1\mu m$ and $\epsilon = 3\mu m$ respectively at streamwise location $i = 140$. (upper figure: $\epsilon = 0.1\mu m$, mid figure: $\epsilon = 1\mu m$, lower figure: $\epsilon = 3\mu m$.)

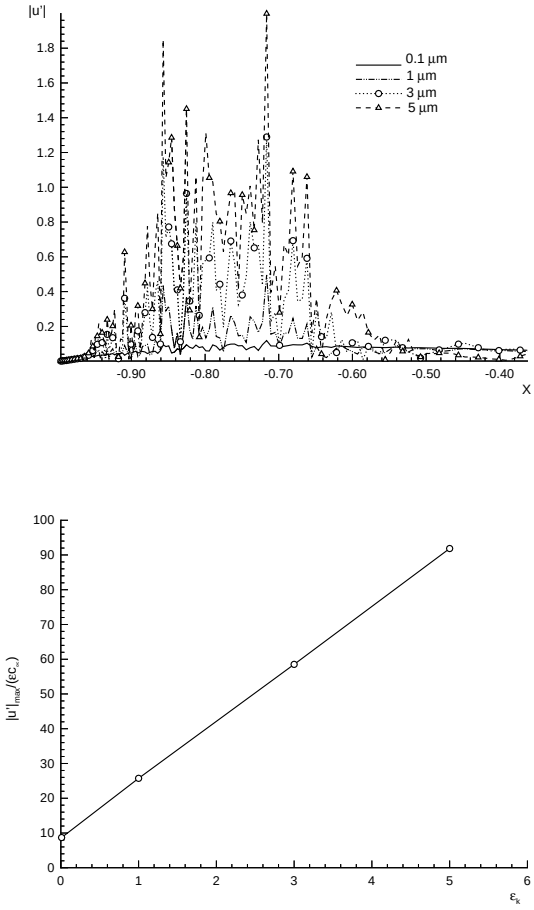

Figure 28: Comparison of $|u'|_{max}$ distributions along x (upper figure) and $|u'|_{max}/(\epsilon C_\infty)$ for different roughness amplitude ϵ_k (lower figure) at $\beta = 0.18$.

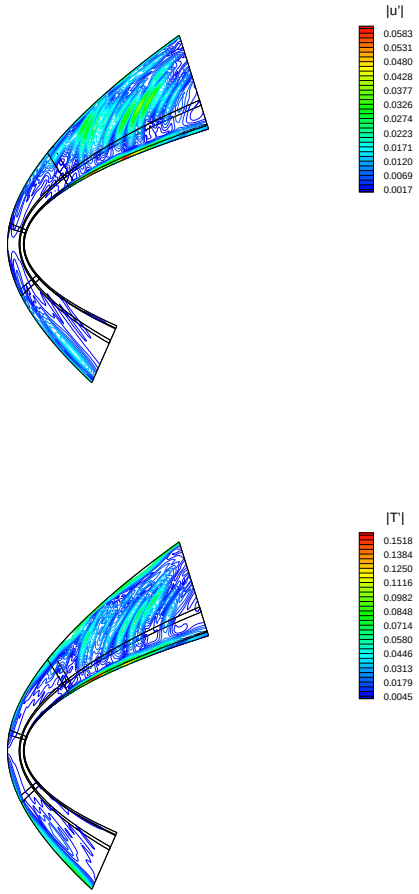

Figure 29: Fourier amplitude $|u'|$ and $|T'|$ contours for the receptivity to vorticity waves with random roughness $\epsilon_k = 3\mu m$ at $\omega = 20$ and $\beta = 0.18$.

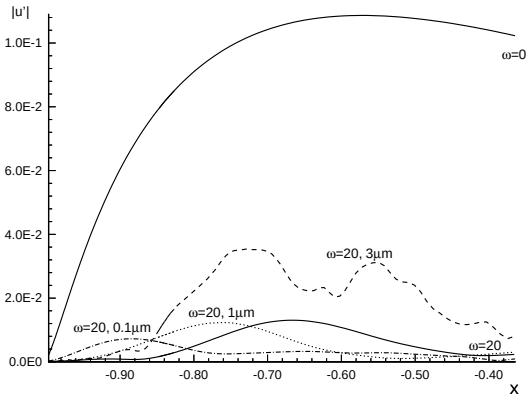

Figure 30: Comparisons of $|u'|_{max}$ distributions along x for different amplitudes of surface roughness with or without traveling waves with $\omega = 20$ in spanwise direction.

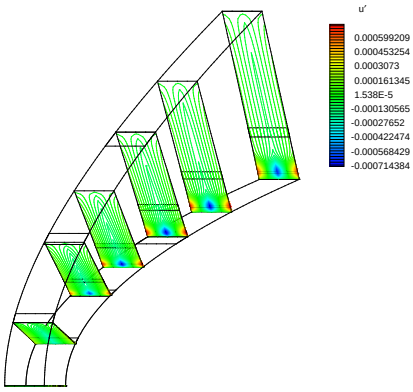

Figure 31: 3-D instantaneous u' contours of the receptivity to standing entropy waves with wavenumber $\beta = 0.18$.

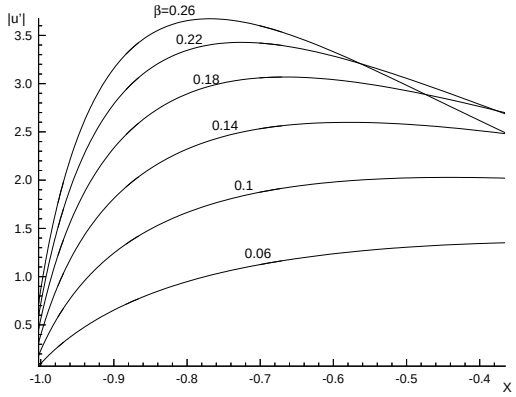

Figure 33: Comparisons of the maximum | u' | distributions for different wavenumber, β.

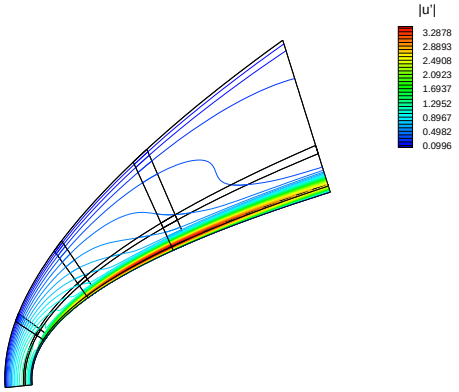

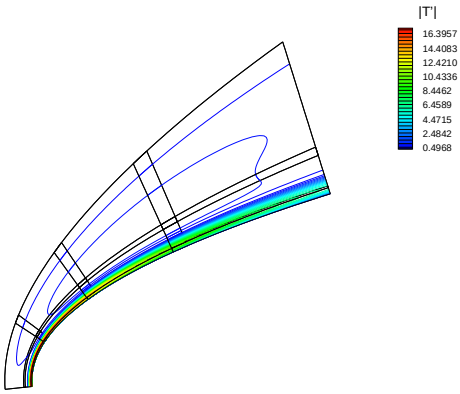

Figure 32: Fourier amplitude $|u'|$ and $|T'|$ contours for the receptivity to standing entropy waves at $\beta = 0.22$.

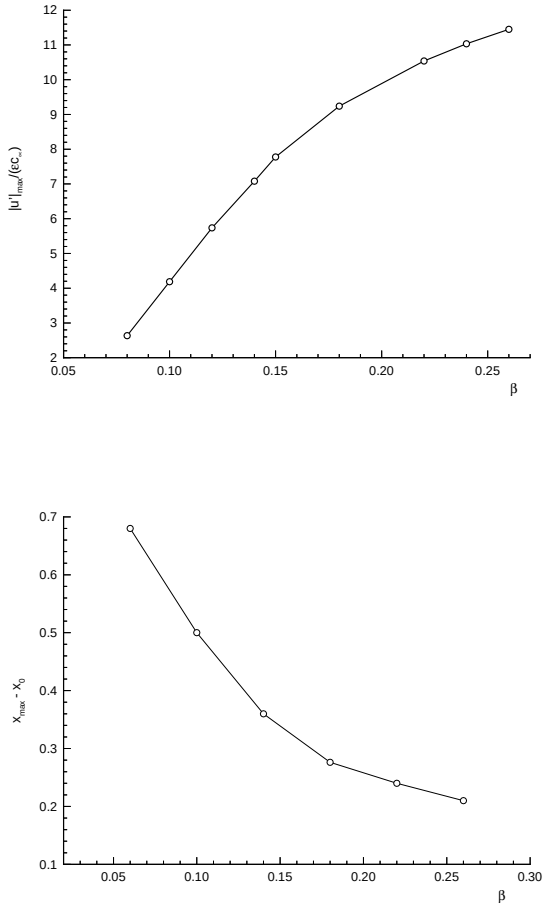

Figure 34: Comparisons of the ratios of $|u'|_{max}$ to the amplitude of freestream disturbances with wavenumbers, β, (upper figure) and the locations of the peaks vs. β (lower figure).